SENSITIVITY-INFORMED IDENTIFICATION OF TEMPERATURE-DEPENDENT PIEZOELECTRIC MATERIAL PARAMETERS

RAPHAEL KUESS[a], OLGA FRIESEN[b], LEANDER CLAES[b], AND ANDREA WALTHER[a]

[a]*Humboldt-Universität zu Berlin, Institut für Mathematik, 10099 Berlin, Germany*
[b]*Universität Paderborn, Institut für Elektrotechnik und Informationstechnik, 33098 Paderborn, Germany*

ABSTRACT. An accurate characterization of temperature-dependent material parameters of piezoceramics is crucial for the design and simulation of reliable sensors and actuators. This characterization is typically formulated as an ill-posed inverse problem, which is challenging to solve not only because of its ill-posedness, but also because of parameter sensitivities, which vary by several orders of magnitude and exhibit a strong coupling between parameters. For this reason we propose a *block coordinate descent* (BCD) framework combined with a *globalized regularized structure exploiting* (GRSE) Quasi-Newton method. A systematic sensitivity-driven strategy for the optimal partitioning of material parameters into blocks is established. By analyzing first- and second-order sensitivity information, our method identifies blocks that minimize inter-block coupling and group parameters with similar sensitivity profiles. Subsequent to a finite element discretization, the derivatives required for both the sensitivity analysis and the optimization are computed accurately using algorithmic differentiation. The proposed BCD-GRSE method is validated through a numerical experiment with noisy synthetic data. Finally, we present the reconstruction results for the piezoelectric material parameters of an annular sample based on physical measurement data.

Key words: inverse parameter identification, sensitivity analysis, piezoelectricity, block coordinate descent, regularized Quasi-Newton
MSC 2020: 74J25, 90C31, 49M15, 74M05, 35R30

1. INTRODUCTION

Piezoelectric components are essential in a vast array of electronic devices, ranging from everyday items such as lighters and headphones to advanced medical and industrial applications like ultrasound imaging and ultrasonic bonding. Thoroughly understanding the behavior of these materials is crucial for designing high-performance devices, particularly given the temperature-dependent electromechanical characteristics of these components. Piezoelectric ceramics undergo changes in behavior due to heating during operation, especially in high-power ultrasound applications, resulting in a shift in the resonance at which the device operates. While the effects of temperature are the primary influence considered in this work, it should be noted that mechanical stresses and electrical biasing conditions present during operation can also affect the resonance behavior. Therefore, our aim is to develop a method for accurately predicting these changes to ensure device reliability and performance. Consequently, an optimization technique is required to determine the complete set of temperature-dependent material parameters (elastic, piezoelectric, and dielectric) from experimental measurements. This problem is formulated as an inverse problem, which is challenging for several reasons. It is ill-posed in the sense of Hadamard, i.e., the solution may not be unique or does not depend continuously on the data, necessitating regularization to ensure a stable and physically meaningful solution. Furthermore, the problem is characterized by strong coupling and very different orders of magnitude between different material parameters. Additionally, the sensitivities of the forward operator with respect to different parameters can vary by several orders of magnitude as well. To address these challenges, we propose an optimization framework based on a *Block Coordinate Descent* (BCD) strategy, where the parameters are partitioned based on a sensitivity and cross-sensitivity analysis. Within each block update, we employ the *regularized structure-exploiting Powell-Symmetric-Broyden* (RSE-PSB) method, see [23], that efficiently handles the remaining non-linearity and intra-block parameter coupling by incorporating second-order derivative information.

Date: February 12, 2026.

Corresponding author: Raphael Kuess, raphael.kuess@hu-berlin.de.

Related Work. Inverse material parameter identification for piezoelectric materials is a well-established field. Common approaches involve minimizing the discrepancy between measured and simulated electrical impedance using Landweber or Gauss-Newton methods [18, 25]. Furthermore, identifying only those parameters to which the impedance is most sensitive in specific frequency ranges while keeping others fixed is discussed in [6]. While effective to some extent, this approach neglects parameter interactions that occur across different frequency bands. In other studies, Sobol's method was used as an alternative approach for calculating sensitivities [2]. A significant challenge arises due to the low sensitivity of the impedance to certain parameters. To enhance sensitivity, optimization of the geometry of the electrodes is investigated in [19]. The application of BCD methods to piezoelectric parameter identification was successfully explored by [7, 8, 18]. The first two focus on the inverse characterization of piezoelectric materials considering only a single disc specimen. Both works address the known sensitivity issues of disc-shaped samples with electrodes fully covering both faces and propose a customized triple-ring electrode topology to increase the sensitivity. Then, in [8], certain parameters are optimized in frequency ranges where sensitivities are high only for that parameter, while in [7], parameter updates are performed sequentially. In the specific case of piezoceramic rings, it has been observed that the optimization of electrode topology is no longer necessary, as the sensitivity with respect to particular parameters is already increased by the given geometry compared to a piezoceramic disc [10]. The material parameters influenced by temperature [12], electrical [11], and mechanical loads [13, 14, 30] were identified through the application of the above-mentioned methods. The temperature-dependent material parameters were additionally identified by implementing a neural network for initial estimates, followed by the application of an inverse procedure as a final optimization step [5]. Although satisfactory results have been achieved, cross-sensitivities are only implicitly addressed, and an algorithmic mechanism for dealing with the highly divergent sensitivities in the optimization routine and parameter coupling that fundamentally characterize this inverse problem has been barely discussed. Hence, a thorough grouping of parameters into blocks has not been developed so far. Consequently, we will propose an algorithmic approach to group the parameters in Section 3.

Contribution. In this paper, we develop a rigorous and practically applicable approach for identifying temperature-dependent piezoelectric material parameters using only a single ring-shaped sample. First, we analyze the inverse problem of identifying temperature-dependent piezoelectric parameters in the frequency domain. The analysis covers the parameter-to-state map, Fréchet differentiability of the forward operator and the well-posedness of the continuous adjoint problem for all excitation frequencies. This provides the mathematical foundation for the discretize-then-optimize approach. Then, we propose a sensitivity-informed BCD framework for solving ill-posed inverse problems. Therein, we analyze first-order sensitivities, total sensitivities, cross-sensitivities, and a curvature-based intra-block roughness measure derived from second-order information. Based on these measures we present a systematic methodology to partition material parameters for the BCD algorithm into blocks, which uses first- and second-order sensitivity analysis to minimize the inter-block coupling (cross-sensitivity), while maintaining intra-block numerical stability (roughness). Subsequently, we combine the sensitivity-driven BCD framework with the RSE-PSB method and its globalized version (GRSE), which are analyzed from a theoretical perspective in [23]. The proposed BCD-GRSE algorithm, which was validated using synthetic noisy data, demonstrates its ability to accurately reconstruct all piezoelectric material parameters, even those with very low sensitivity. Finally, we present the reconstruction results for the material parameters of an annular PIC181 sample (*PI Ceramic, Germany*) with inner radius of $2.6\,\mathrm{mm}$, outer radius of $6.35\,\mathrm{mm}$ and thickness of $1\,\mathrm{mm}$, based on experimental measurement data across a temperature range of $25\,^\circ\mathrm{C}$ – $85\,^\circ\mathrm{C}$. Using the reconstructed parameters, a substantial decrease in the data misfit is achieved, obtaining full temperature-dependent material descriptions from a single specimen.

Structure of the paper. Section 2 details the mathematical modeling, starting with the forward problem formulation. The operators of the inverse problem are defined and the derivation and analysis of the continuous adjoint system follows. Section 3 presents our proposed numerical solution strategy. We introduce the RSE-PSB quasi-Newton method and embed it within the BCD framework. Next, the sensitivity-driven methodology for optimal block partitioning is discussed and the simulation-based inverse problem with synthetic data is solved in Section 4. Section 5 describes the experimental setup for measuring temperature-dependent impedance data and presents the results of applying our method to real-world measurements. Conclusions and an outlook are given in Section 6.

2. MODELING AND ANALYSIS OF THE INVERSE PROBLEM

2.1. **Modeling of the forward problem.** For practical applications, thin, annular piezoelectric components with inner radius r_1, outer radius r_2, radial length $l = r_2 - r_1$ and height/thickness $h < l$, as illustrated in Figure 1, are the objects of high interest. We denote the geometry of the considered piezoceramic with a three-dimensional bounded domain $\Omega_{3\mathrm{d}} \subset \mathbb{R}^3$, i.e., $\Omega_{3\mathrm{d}}$ is a non-empty connected open subset of $\mathbb{R}^3$. This axisymmetric assumption reduces the computational complexity of the model from a three-dimensional (3D) to a two-dimensional (2D) problem, while accurately capturing the relevant physical properties. Consequently, it is advantageous to utilize the symmetry of the geometry and to use the cylindrical instead of the Cartesian coordinate system. Hence, we obtain a rectangular Lipschitz domain $\Omega \subset \mathbb{R}^2$, where its boundary $\partial\Omega$ can be represented as the disjoint union $\partial\Omega := \Gamma_{\mathrm{a}} \dot{\cup} \Gamma_0 \dot{\cup} \Gamma_{\mathrm{n}}$. Here, Γ_{a} describes the boundary segment which is excited electrically with an excitation signal independent of the spatial domain (equally distributed) and Γ_0 refers to the boundary segment which is grounded. This can be modeled in the system of partial differential equations (PDEs) as Dirichlet boundary conditions. The segment Γ_{n} constitutes the remaining boundary of $\partial\Omega$ and is included in the PDE model by Neumann boundary conditions. Furthermore, we denote the non-empty mixed Dirichlet boundary with $\Gamma_{\mathrm{d}} := \Gamma_{\mathrm{a}} \dot{\cup} \Gamma_0$, i.e., $\partial\Omega := \Gamma_{\mathrm{d}} \dot{\cup} \Gamma_{\mathrm{n}}$. Assuming an initial stationary system, a macroscopic approach is adopted. In the context of piezoelectric systems, the mechanical and electrical quantities are interconnected by the principle of thermodynamic equilibrium. The first law of thermodynamics must be considered. Hence, a contribution of free energy is required, which is obtained by a Legendre transformation of the internal energy. It is noteworthy that a variety of energy forms, such as Gibbs free energy, Helmholtz free energy, and different enthalpy forms, can be utilized to derive the constitutive equations. However, these constitutive equations are found to be equivalent. The material parameters $c^{\mathrm{E}}(\theta)$, $e(\theta)$ and $\epsilon^{\mathrm{S}}(\theta)$ contained therein are represented as temperature-dependent matrix-valued functions that describe the material behavior of the piezoceramic under consideration. This approach offers valuable insights into the behavior of piezoelectric materials at varying temperatures, which are crucial in thermal coupling models. Given that temperatures are typically non-linear and continuous functions, non-linearity emerges at this point. Applying a Taylor series expansion to the Gibbs free energy yields the following linear constitutive laws.

Definition 2.1 (Constitutive laws)**.** The so-called e-form of the piezoelectric coupled constitutive equations reads as

$$\sigma = c^{\mathrm{E}}(\theta) \cdot S - e(\theta) \cdot E, \quad D = e(\theta) \cdot S + \epsilon^{\mathrm{S}}(\theta) \cdot E,$$

where $\cdot$ denotes the inner product in finite dimensional linear spaces, σ the mechanical stress, c^{E} the elastic stiffness parameter, S the mechanical strain, e the piezoelectric coupling parameter, D the dielectric displacement, ϵ^{S} the permittivity parameter, and E the electric field.

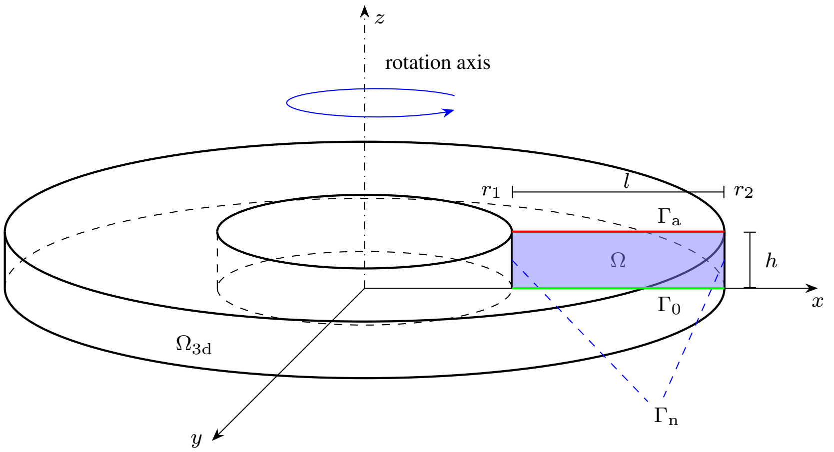

FIGURE 1. Geometric model of an annular piezoelectric specimen (3D geometry $\Omega_{3\mathrm{d}}$) with its cross-section, i.e., the 2D domain Ω derived from the axisymmetric domain $\Omega_{3\mathrm{d}}$.

The superscripts E and S in the material parameters c^{E} and ϵ^{S} signal that these quantities are understood under conditions of constant electric field and constant mechanical strain, respectively. In the first constitutive equation, the first term can be identified as Hooke's law and the second term as the inverse piezoelectric effect. The second constitutive equation is structured similarly, with the first term representing the direct piezoelectric effect and the second term describing the dielectric behavior of the material. Then, the constitutive laws are coupled to the equilibrium equations, namely Newton's second law of motion for mechanical behavior and Gauss's law, as well as to the field equations, i.e., Faraday's law and the displacement gradient, where we consider the differential operators

$$\nabla := \begin{pmatrix} \frac{\partial}{\partial r} \\ \frac{\partial}{\partial z} \end{pmatrix} \quad \text{and} \quad \mathcal{B} = \begin{pmatrix} \frac{\partial}{\partial r} & 0 \\ \frac{1}{r} & 0 \\ 0 & \frac{\partial}{\partial z} \\ \frac{\partial}{\partial z} & \frac{\partial}{\partial r} \end{pmatrix}$$

in Voigt notation transformed to cylindrical coordinates. We denote the normal vector corresponding to ∇ with n and the normal element corresponding to $\mathcal{B}$ with $\mathcal{N}$.

Remark 2.2. Note, that the coordinate transformation from Cartesian to cylindrical coordinates is a smooth diffeomorphism and hence isometrically isomorphic. Consequently, the operators above are transformations of the corresponding operators in [22].

In order to model the physical behavior more reliably, it is necessary to include a damping model. In this context, we assume only the occurrence of mechanical friction for which a simplified model, namely the Rayleigh damping model is employed in the mechanical equation. The Rayleigh damping model introduces two parameters, α and β, which represent mass-proportional and stiffness-proportional damping, respectively. This is a common simplification to describe energy dissipation within the material during elastic processes [9]. Hence, we obtain the transient piezoelectric system for each fixed temperature θ

$$\begin{aligned} \rho\ddot{u} + \alpha\rho\dot{u} - \mathcal{B}^{\mathrm{T}}\left(c^{\mathrm{E}}(\theta)\mathcal{B}u + \beta c^{\mathrm{E}}(\theta)\mathcal{B}\dot{u} + e(\theta)^{\mathrm{T}}\nabla\phi\right) &= 0 && \text{in } \Omega \times (0,T) \\ -\nabla\cdot\left(e(\theta)\mathcal{B}u - \epsilon^{\mathrm{S}}(\theta)\nabla\phi\right) &= 0 && \text{in } \Omega \times (0,T) \\ \phi &= 0 && \text{on } \Gamma_0 \times (0,T) \\ \phi &= \phi^{\mathrm{e}} && \text{on } \Gamma_{\mathrm{a}} \times (0,T) \\ n\cdot\left(e(\theta)\mathcal{B}u - \epsilon^{\mathrm{S}}(\theta)\nabla\phi\right) &= 0 && \text{on } \Gamma_{\mathrm{n}} \times (0,T) \\ \mathcal{N}^{\mathrm{T}}\left(c^{\mathrm{E}}(\theta)\mathcal{B}u + \beta c^{\mathrm{E}}(\theta)\mathcal{B}\dot{u} + e(\theta)^{\mathrm{T}}\nabla\phi\right) &= 0 && \text{on } \partial\Omega \times (0,T) \\ u(t=0) &= u_0 && \text{in } \Omega \times \{0\} \\ \dot{u}(t=0) &= u_1 && \text{in } \Omega \times \{0\}\,, \end{aligned}$$

where T is the end time of the observed time period, $\alpha, \beta \in \mathbb{R}_0^+$ are the Rayleigh damping parameters, $\rho \in \mathbb{R}^+$ is the mass density and $\phi^{\mathrm{e}} \in H^1(0,T)$ is a known excitation function. The sought-after parameters $c^{\mathrm{E}}(\theta), e(\theta)$, and $\epsilon^{\mathrm{S}}(\theta)$ are bounded linear operators defined as follows.

Definition 2.3 (Material parameter functions)**.** Let $\Theta \in \mathbb{R}^+$ be a bounded temperature domain and $\eta \in \mathbb{R}^+$. Then we define the elasticity parameter as a matrix-valued function

$$c^{\mathrm{E}}(\theta) := \begin{pmatrix} c_{11}(\theta) & c_{12}(\theta) & c_{13}(\theta) & 0 \\ c_{12}(\theta) & c_{11}(\theta) & c_{13}(\theta) & 0 \\ c_{13}(\theta) & c_{13}(\theta) & c_{33}(\theta) & 0 \\ 0 & 0 & 0 & c_{44}(\theta) \end{pmatrix},$$

where c_{12} and c_{13} are positive functions,

$$c_{11}(\theta) > \eta + c_{12}(\theta), \;\; c_{44}(\theta) > \eta, \;\; c_{33}(\theta) > c_{13}(\theta) + \eta, \;\; c_{11}(\theta) + c_{12}(\theta) \geq 2c_{13}(\theta)$$

and $c_{11}, c_{12}, c_{13}, c_{33}, c_{44} \in L^2(\Theta, \mathbb{R})$, the piezoelectric coupling parameter as a matrix-valued function

$$e(\theta) := \begin{pmatrix} 0 & 0 & 0 & e_{15}(\theta) \\ e_{31}(\theta) & e_{31}(\theta) & e_{33}(\theta) & 0 \end{pmatrix},$$

where $e_{15}, e_{31}, e_{33} \in L^2(\Theta, \mathbb{R})$, and the permittivity parameter as a matrix-valued function

$$\epsilon^{\mathrm{S}}(\theta) := \begin{pmatrix} \epsilon_{11}(\theta) & 0 \\ 0 & \epsilon_{33}(\theta) \end{pmatrix},$$

where $\epsilon_{11}(\theta) > \eta, \ \ \epsilon_{33}(\theta) > \eta$ and $\epsilon_{11}, \epsilon_{33} \in L^2(\Theta, \mathbb{R})$.

These conditions can be seen as sufficient conditions to obtain thermodynamic stability, as they ensure that the strain energy density is positive definite, guaranteeing that the material is physically stable. This can be seen by the following lemma.

Lemma 2.4. *The material parameters $c^{\mathrm{E}}(\theta)$ and $\epsilon^{\mathrm{S}}(\theta)$ defined in Definition 2.3 are uniformly invertible with bounded inverse.*

Proof. The conditions for $\epsilon(\theta)$ are obvious. For $c^{\mathrm{E}}(\theta)$ we compute the eigenvalues

$$\begin{aligned}
\lambda_1(\theta) &= c_{11}(\theta) - c_{12}(\theta) \\
\lambda_2(\theta) &= \frac{1}{2}\left(c_{11}(\theta) + c_{12}(\theta) + c_{33}(\theta) - \sqrt{(8(c_{13}(\theta))^2 + (c_{11}(\theta) + c_{12}(\theta) - c_{33}(\theta))^2)}\right) \\
\lambda_3(\theta) &= \frac{1}{2}\left(c_{11}(\theta) + c_{12}(\theta) + c_{33}(\theta) + \sqrt{(8(c_{13}(\theta))^2 + (c_{11}(\theta) + c_{12}(\theta) - c_{33}(\theta))^2)}\right) \\
\lambda_4(\theta) &= c_{44}(\theta), \ \lambda_5(\theta) = c_{44}(\theta), \ \lambda_6(\theta) = \frac{1}{2}\left(c_{11}(\theta) - c_{12}(\theta)\right).
\end{aligned}$$

Hence $\lambda_1(\theta), \lambda_4(\theta), \lambda_5(\theta) > \eta$ and $\lambda_6(\theta) > \frac{\eta}{2}$. Furthermore, it holds that

$$\lambda_3(\theta) = \frac{1}{2}\left(c_{11}(\theta) + c_{12}(\theta) + c_{33}(\theta) + \sqrt{(8(c_{13}(\theta))^2 + (c_{11}(\theta) + c_{12}(\theta) - c_{33}(\theta))^2)}\right) > \frac{\eta + \eta}{2} = \eta.$$

As $c_{11}(\theta) + c_{12}(\theta) \geq 2c_{13}(\theta))$, it holds that $1 \geq \frac{2c_{13}(\theta))}{c_{11}(\theta)+c_{12}(\theta)}$, which yields

$$c_{33}(\theta) > c_{13}(\theta)) + \eta > \frac{2(c_{13}(\theta))^2}{c_{11}(\theta) + c_{12}(\theta)} + \eta.$$

Hence, we obtain

$$\begin{aligned}
\lambda_2(\theta) &= \frac{1}{2}\left(c_{11}(\theta) + c_{12}(\theta) + c_{33}(\theta) - \sqrt{(8(c_{13}(\theta))^2 + (c_{11}(\theta) + c_{12}(\theta) - c_{33}(\theta))^2)}\right) \\
&> \frac{1}{2}\left(c_{11}(\theta) + c_{12}(\theta) + \frac{2(c_{13}(\theta))^2}{c_{11}(\theta) + c_{12}(\theta)} + \eta \right. \\
&\qquad \left. - \sqrt{(8(c_{13}(\theta))^2 + (c_{11}(\theta) + c_{12}(\theta) - \frac{2(c_{13}(\theta))^2}{c_{11}(\theta) + c_{12}(\theta)} - \eta)^2)}\right) \\
&> \frac{1}{2}\left(c_{11}(\theta) + c_{12}(\theta) + \frac{2(c_{13}(\theta))^2}{c_{11}(\theta) + c_{12}(\theta)} + \eta \right. \\
&\qquad \left. - \sqrt{(8(c_{13}(\theta))^2 + (c_{11}(\theta) + c_{12}(\theta) - \frac{2(c_{13}(\theta))^2}{c_{11}(\theta) + c_{12}(\theta)})^2)}\right) \\
&> \frac{1}{2}\left(c_{11}(\theta) + c_{12}(\theta) + \frac{2(c_{13}(\theta))^2}{c_{11}(\theta) + c_{12}(\theta)} + \eta \right. \\
&\qquad \left. - \sqrt{\frac{((c_{11}(\theta))^2 + 2c_{11}(\theta)c_{12}(\theta) + (c_{11}(\theta))^2 + 2(c_{13}(\theta))^2)^2}{(c_{11}(\theta) + c_{12}(\theta))^2}}\right) > \frac{\eta}{2}.
\end{aligned}$$

It follows that if the conditions above are satisfied then $c(\theta)$ has eigenvalues bounded away from 0. □

Hence, we define for some $\eta > 0$

$$\tilde{X} := \left\{ p = (c^{\mathrm{E}}(\theta), e(\theta), \epsilon^{\mathrm{S}}) \in L^2(\Theta, \mathbb{R}^{4\times 4}) \times L^2(\Theta, \mathbb{R}^{2\times 4}) \times L^2(\Theta, \mathbb{R}^{2\times 2}) \right\},$$

which is isometrically isomorphic to the parameter space

$$\begin{aligned} X := & \Big\{ p \in L^2(\Theta, \mathbb{R})^{10} : \; p_1 = c_{11}(\theta), \; p_2 = c_{12}(\theta), \; p_3 = c_{13}(\theta), \; p_4 = c_{33}(\theta), \; p_5 = c_{44}(\theta), \\ & \quad p_6 = \epsilon_{11}(\theta), \; p_7 = \epsilon_{33}(\theta), \; p_8 = e_{15}(\theta), \; p_9 = e_{31}(\theta), \; p_{10} = e_{33}(\theta) \Big\}. \end{aligned} \tag{2.1}$$

Similarly to [22], we homogenize the mixed Dirichlet boundary conditions using the Dirichlet lift Ansatz. This is a standard technique to transform a problem with non-homogeneous Dirichlet boundary conditions into an equivalent formulation with homogeneous boundary conditions. The resulting homogeneous problem is more convenient for theoretical analysis, particularly to prove well-posedness of the forward problem. As $\Gamma_a \cap \Gamma_0 = \emptyset$, Ω is a Lipschitz domain and $\phi^e \in H^1(0,T)$, we use Remark 2.2 to apply Remark 3.5 in [22], yielding that there exists a $\chi \in H^1\left(0, T; H^2(\Omega, \mathbb{R})\right))$ with the property that

$$\mathrm{Tr}(\chi(t)) = \begin{cases} \phi_e(t) & \text{on } \Gamma_a \\ 0 & \text{on } \Gamma_0 \end{cases} \quad \text{a.e. in time.} \tag{2.2}$$

Hence, with

$$\phi_0(t) \in H^2_{0,\Gamma}(\Omega, \mathbb{R}) = \left\{ g \in H^2(\Omega, \mathbb{R}) \mid \quad g\big|_{(\Gamma_\mathrm{a} \cup \Gamma_0)} = 0 \right\},$$

we reformulate ϕ as $\phi(t) = \phi_0(t) + \chi(t)$ a.e. in time and obtain the piezoelectric dynamical system

$$\rho \ddot{u} + \alpha \rho \dot{u} - \mathcal{B}^T \left(c^E \mathcal{B} u + \beta c^E \mathcal{B} \dot{u} + e^T \nabla \phi_0 \right) = \mathcal{B}^T e^T \nabla \chi \qquad \text{in } \Omega \times (0,T) \tag{2.3}$$

$$-\nabla \cdot (e \mathcal{B} u - \epsilon \nabla \phi_0) = -\nabla \cdot \epsilon \nabla \chi \qquad \text{in } \Omega \times (0,T) \tag{2.4}$$

$$n \cdot (e \mathcal{B} u - \epsilon \nabla \phi_0) = n \cdot \epsilon \nabla \chi \qquad \text{on } \Gamma_n \times (0,T) \tag{2.5}$$

$$\mathcal{N}^T \left(c^E \mathcal{B} u + \beta c^E \mathcal{B} \dot{u} + e^T \nabla \phi_0 \right) = -\mathcal{N}^T e^T \nabla \chi \qquad \text{on } \partial\Omega \times (0,T) \tag{2.6}$$

$$u(t=0) = u_0 \qquad \text{in } \Omega \tag{2.7}$$

$$\dot{u}(t=0) = u_1 \qquad \text{on } \Omega. \tag{2.8}$$

We will use results of [22] to obtain unique solutions. For this purpose, we define the space

$$H^2_{\mathcal{B}}(\Omega, \mathbb{R}^2) = \left\{ g \in L^2(\Omega, \mathbb{R}^2) \mid \quad \|g\|_{H^2_{\mathcal{B}}(\Omega,\mathbb{R}^2)} := \|g\|_{L^2(\Omega,\mathbb{R}^2)} + \|\mathcal{B} g\|_{L^2(\Omega,\mathbb{R}^2)} + \left\|\mathcal{B}^\mathrm{T} \mathcal{B} g\right\|_{L^2(\Omega,\mathbb{R}^2)} \right\}.$$

Corollary 2.5. There exists a unique solution

$$(u, \phi_0) \in L^2(0, T; H^2_{\mathcal{B}}(\Omega, \mathbb{R}^2)) \times L^2(0, T; H^2_{0,\Gamma}(\Omega, \mathbb{R})) \tag{2.9}$$

with

$$\dot{u} \in L^2(0, T; H^2_{\mathcal{B}}(\Omega, \mathbb{R}^2)) \quad \text{and} \quad \ddot{u} \in L^2(0, T; H^2_{\mathcal{B}}(\Omega, \mathbb{R}^2)^*) \tag{2.10}$$

to the system (2.3)-(2.8).

Proof. Remark 2.2 allows to apply Corollary 3.7 in [22] with $a \equiv f \equiv g \equiv 0$. Since for each $\theta \in \Theta$, the material parameters are constant, they satisfy the regularity conditions of Corollary 3.7 in [22]. Furthermore, Assumption 2.2 in [22] is fulfilled due to Lemma (2.4). Using $m = 2$ in Corollary 3.7 of [22] concludes the proof, due to the assumed regularity of ϕ_e and χ. ☐

Note that the higher regularities in space of the solutions are needed to provide well-definedness of the observation operator, see subsection 2.2. To simplify the PDE and to deal better with measurements the whole system will be considered in a time-harmonic setting and thus in frequency domain. For this purpose, we assume that the body is initially at rest, i.e., at $t = 0$ the piezoelectric specimen is not vibrating, stretching or compressing ($u_0 = u_1 = 0$), and apply a Fourier transformation to the system (2.3)-(2.8).

Hence, we obtain the time-harmonic PDE

$$\forall\omega \in \mathcal{W}: \; -\rho\omega^2 s_1\hat{u} - \mathcal{B}^{\mathrm{T}}\left(s_2 c^{\mathrm{E}}(\theta)\mathcal{B}\hat{u} + e(\theta)^{\mathrm{T}}\nabla\hat{\phi}_0\right) = \mathcal{B}^{\mathrm{T}} e(\theta)^{\mathrm{T}}\nabla\hat{\chi} \quad \text{in } \Omega \tag{2.11}$$

$$-\nabla\cdot\left(e(\theta)\mathcal{B}\hat{u} - \epsilon^{\mathrm{S}}(\theta)\nabla\hat{\phi}_0\right) = -\nabla\cdot\epsilon^{\mathrm{S}}(\theta)\nabla\hat{\chi} \quad \text{in } \Omega \tag{2.12}$$

$$n\cdot\left(e(\theta)\mathcal{B}\hat{u} - \epsilon^{\mathrm{S}}(\theta)\nabla\hat{\phi}_0\right) = n\cdot\epsilon^{\mathrm{S}}(\theta)\nabla\hat{\chi} \quad \text{on } \Gamma_{\mathrm{n}} \tag{2.13}$$

$$\mathcal{N}^{\mathrm{T}}\left(s_2 c^{\mathrm{E}}(\theta)\mathcal{B}\hat{u} + e(\theta)^{\mathrm{T}}\nabla\hat{\phi}_0\right) = -\mathcal{N}^{\mathrm{T}} e(\theta)^{\mathrm{T}}\nabla\hat{\chi} \quad \text{on } \partial\Omega, \tag{2.14}$$

where $s_1 := 1 - \mathrm{i}\frac{\alpha}{\omega}$, $s_2 := 1 + \mathrm{i}\omega\beta$ and $(\hat{u}, \hat{\phi}_0) \in H^2_{\mathcal{B}}(\Omega, \mathbb{C}^2) \times H^2_{0,\Gamma}(\Omega, \mathbb{C})$ is the solution of the system above. We denoted the space of angular frequencies with $\mathcal{W} \subset \mathbb{R}^+$, $|\mathcal{W}| < \infty$. Transforming the system to the frequency domain via Fourier transformation converts time-derivatives into algebraic multiplications by $\mathrm{i}\omega$, where i is the imaginary unit, $\omega = 2\pi f$ is the angular frequency and $f \in \mathcal{F} \subset \mathbb{R}^+$ is the frequency. This approach recasts the time-dependent PDEs into a set of stationary, complex-valued PDEs, one for each angular frequency ω of interest. This formulation is computationally advantageous as it allows us to solve a series of smaller, independent problems rather than a single large time-dependent one.

Theorem 2.6. *There exists a unique solution*

$$(u, \phi_0) \in H^2_{\mathcal{B}}(\Omega, \mathbb{C}^2) \times H^2_{0,\Gamma}(\Omega, \mathbb{C}) \tag{2.15}$$

to the system (2.11) - (2.14).

Proof. By Corollary 2.5, the transient system (2.3)-(2.8) with $u_0 = u_1 = 0$ admits a unique solution

$$(u, \phi_0) \in L^2(0, T; H^2_{\mathcal{B}}(\Omega, \mathbb{R}^2)) \times L^2(0, T; H^2_{0,\Gamma}(\Omega, \mathbb{R})).$$

Fourier transforming this solution in time yields

$$\hat{u}(\omega) := \int_0^T u(t)e^{-i\omega t}\,\mathrm{d}t\,, \quad \hat{\phi}_0(\omega) := \int_0^T \phi_0(t)e^{-i\omega t}\,\mathrm{d}t\,.$$

Due to Plancherel's Theorem, see [4, Chapter 7] or [21, Theorem 2.20], the Fourier transformation is continuously invertible on $L^2(0, T)$, or $L^2(0, T; H)$ for any separable Hilbert space H, respectively. Consequently, the Fourier transformed solution $(\hat{u}, \hat{\phi}_0)$ of system (2.3)-(2.8) is well-defined in

$$H^2_{\mathcal{B}}(\Omega, \mathbb{C}^2) \times H^2_{0,\Gamma}(\Omega, \mathbb{C}).$$

Similarly, Fourier transforming the Dirichlet Lift function χ yields $\hat{\chi} \in H^2(\Omega, \mathbb{C})$ with the property that

$$\mathrm{Tr}(\hat{\chi}) = \begin{cases} \hat{\phi}^{\mathrm{e}} & \text{on } \Gamma_{\mathrm{a}} \\ 0 & \text{on } \Gamma_0, \end{cases}$$

where $\hat{\phi}^{\mathrm{e}}$ is the Fourier transformed excitation signal ϕ^{e} and $\hat{\phi} = \hat{\phi}_0 + \hat{\chi}$. Hence, the time-dependent system (2.3)-(2.8) Fourier transforms to (2.11) - (2.14). Consequently, the Fourier transformed unique time-domain solution $\hat{u}$ and $\hat{\phi}_0$ provides a solution to the frequency-domain PDE (2.11) - (2.14) for each $\omega \in \mathcal{W}$. These solutions are unique as supposing otherwise, i.e., $(\tilde{u}(\omega), \tilde{\phi}_0(\omega))$ is another solution of the frequency-domain system for the same $\omega \in \mathcal{W}$, yields that the inverse Fourier transform of $(\tilde{u}(\omega), \tilde{\phi}_0(\omega))$ would define another solution of system (2.3)-(2.8), contradicting Corollary 2.5. This proves both existence and uniqueness of the solution in the frequency domain. □

Considering the weak form of the system (2.11) - (2.14) via the operators

$$\begin{aligned} B((p,z),(v,w)) = 2\pi\int_\Omega \Big(&-s_1\rho\omega^2\hat{u}^{\mathrm{T}}\overline{v} + \left(s_2 c^{\mathrm{E}}(\theta)\mathcal{B}\hat{u} + e(\theta)^{\mathrm{T}}\nabla\hat{\phi}_0\right)^{\mathrm{T}}\overline{\mathcal{B}v} + \\ &\left(e(\theta)\mathcal{B}\hat{u} - \epsilon^{\mathrm{S}}(\theta)\nabla\hat{\phi}_0\right)^{\mathrm{T}}\overline{\nabla w}\Big)\, r\,\mathrm{d}\Omega\,, \end{aligned} \tag{2.16}$$

$$L(v, w) = 2\pi\int_\Omega \left(-(e(\theta)^{\mathrm{T}}\nabla\hat{\chi})^{\mathrm{T}}\overline{\mathcal{B}v} + (\epsilon^{\mathrm{S}}(\theta)\nabla\hat{\chi})^{\mathrm{T}}\overline{\nabla w}\right) r\,\mathrm{d}\Omega\,. \tag{2.17}$$

yields the bilinear operator equation

$$\forall(v,w) \in H^2_{\mathcal{B}}(\Omega,\mathbb{C}^2) \times H^2_{0,\Gamma}(\Omega,\mathbb{C}): \; B((p,z),(v,w)) = L(v,w).$$

Note that the operators in identity (2.16) and (2.17) are the coordinate and Fourier transformed operators corresponding to B and L in [22].

2.2. **Operators of the inverse problem.** To formulate the inverse problem, we discretize the continuous temperature dependency. This allows us to solve the inverse problem for the material parameters at each discrete temperature point. Hence, we denote the discretized temperature interval of finite cardinality as $\Theta \subset \mathbb{R}^+$. Before stating the inverse problem for each temperature point $\theta \in \Theta$, we have to introduce the corresponding operators. For this purpose, we need the parameter space defined in (2.1) and the state space, which coincides with the solution space of the forward problem, i.e., the space of solutions to the system (2.11) - (2.14). Consequently, we obtain the state space

$$W := \left(H^2_{\mathcal{B}}(\Omega,\mathbb{C}^2) \times H^2_{0,\Gamma}(\Omega,\mathbb{C})\right)^{|\mathcal{W}|}.$$

This reflects that for a given parameter p, the forward problem consists of solving the harmonic PDE for each angular frequency $\omega \in \mathcal{W}$ independently. Therefore, a single state $z \in W$ is a collection of solutions $z = \{z_\omega\}_{\omega\in\mathcal{W}}$ with $z_\omega = (\hat{u}_\omega, \hat{\phi}_{0,\omega})$. Then the model operator will be defined as follows.

Definition 2.7 (Model operator)**.** The piezoelectric model operator $A^\theta : X \times W \to W^*$ for a fixed temperature $\theta \in \Theta$ via the bilinear form (2.16) and the linear form (2.17) component wise for each $\omega \in \mathcal{W}$ is given by

$$\begin{aligned}\langle A^\theta_\omega(p,z),(v,w)\rangle_{W^*,W} &:= 2\pi \int_\Omega \Big(- s_1\rho\omega^2\hat{u}^{\mathrm{T}}\overline{v} + \Big(s_2 c^{\mathrm{E}}(\theta)\mathcal{B}\hat{u} + e^{\mathrm{T}}(\theta)\nabla\hat{\phi}_0\Big)^{\mathrm{T}}\overline{\mathcal{B}v} \\ &+ \Big(e(\theta)\mathcal{B}\hat{u} - \epsilon^{\mathrm{S}}(\theta)\nabla\hat{\phi}_0\Big)^{\mathrm{T}}\overline{\nabla w} + (e^{\mathrm{T}}(\theta)\nabla\hat{\chi})^{\mathrm{T}}\overline{\mathcal{B}v} - (\epsilon^{\mathrm{S}}(\theta)\nabla\hat{\chi})^{\mathrm{T}}\overline{\nabla w}\Big) r \,\mathrm{d}(r,z)\,, \end{aligned} \tag{2.18}$$

where we abbreviated $z = (\hat{u}, \hat{\phi}_0)$.

To recover information on the parameter p, we need observations of the state z and the parameter. Hence, we define the measured charge pulse, where we assume that the electrodes are conductive and thus the charge is distributed equally on the loaded electrode.

Definition 2.8 (Observation operator)**.** The measured charge pulse for a fixed temperature $\theta \in \Theta$ is defined component wise for each $\omega \in \mathcal{W}$ by

$$Q^\theta_\omega(p,z) = 2\pi \int_{\Gamma_{\mathrm{a}}} r\left(e(\theta)\mathcal{B}\hat{u} - \epsilon^{\mathrm{S}}(\theta)\nabla\left(\hat{\phi}_0 + \hat{\chi}\right)\right)\cdot n \,\mathrm{d}(r,z)\,. \tag{2.19}$$

Motivated by physical observations, we assume that $\left\|Q^\theta_\omega(p,z)\right\|_{\mathbb{C}} > 0$ for all $(p,z) \in X \times W$ and define the observation operator $C^\theta : X \times W \to \mathbb{R}$ for a fixed temperature $\theta \in \Theta$ component wise for each $\omega \in \mathcal{W}$ as

$$C^\theta_\omega(p,z) = \log\left(\left\|Q^\theta_\omega(p,z)\right\|_{\mathbb{C}}\right). \tag{2.20}$$

The logarithm is applied to the measured quantity to handle the large dynamic range of the electrical charge pulse, which can vary by several orders of magnitude, especially near resonance and anti-resonance frequencies. To model the inverse problem, we employ the reduced approach, meaning that we have to eliminate the model by introducing a so-called parameter-to-state map, which maps the parameter to the weak solution of the underlying PDE model (2.11) - (2.14). This approach implicitly solves the state equation for z given a parameter p, effectively turning the PDE-constrained optimization problem into an unconstrained optimization problem. Hence, it eliminates the state by mapping an arbitrarily fixed parameter p to the corresponding state via the parameter-to-state map S.

Definition 2.9 (Parameter-to-state map)**.** The parameter-to-state map for a fixed temperature $\theta \in \Theta$

$$S^\theta : X \to W, \qquad p \mapsto z,$$

is defined by satisfying the model stated in Definition 2.7, i.e.,

$$\forall z, \zeta \in W : \; [(p,z) \in X \times W \;\wedge\; \langle A^\theta(p,z), \zeta\rangle = 0] \implies z = S^\theta(p),$$

where ζ denotes the test function.

Theorem 2.10. *For each $\theta \in \Theta$ it holds that*

- *the operator A^θ introduced in Definition 2.7 is well-defined, bounded, bijective and continuously Fréchet differentiable on $X \times W$,*
- *the operator C^θ introduced in Definition 2.8 is well-defined, bounded and continuously Fréchet differentiable on $X \times W$, and*
- *the operator S^θ introduced in Definition 2.9 is well-defined, non-linear and continuously Fréchet differentiable on X.*

Proof. Bijectivity of A^θ for each temperature $\theta \in \Theta$ is a direct consequence of Theorem 2.6. Similarly to the proof of Theorem 2.6 we will carry over well-posedness and differentiability results from [22] to the current setting. Hence, we employ the same arguments as in the proof of Theorem 2.6 and subsequently apply Corollary 3.3 to obtain well-definedness. Analogously, invoking the proof of Lemma 4.5 in [22] yields continuous Fréchet differentiability of A^θ with respect to both the parameters and the state, for each temperature $\theta \in \Theta$. Following the same strategy in combination with Lemma 4.5 in [22] yields that S^θ is well-defined and continuously Fréchet differentiable on X for each temperature $\theta \in \Theta$. The non-linearity of S^θ can be obtained from the structure of the model operator. Lastly, using the same arguments as in the proof of Theorem 2.6 again together with Remark 4.6 and $m = 2$ for each $\theta \in \Theta$ implies that the operator Q^θ defined in (2.19) is well-defined, bounded and continuously Fréchet differentiable on $X \times W$ for each temperature $\theta \in \Theta$. As $\left\|Q^\theta_\omega(p,z)\right\|_{\mathbb{C}} > 0$ for each $\omega \in \mathcal{W}$ and the logarithm is smooth on $\mathbb{R}^+$, we deduce that C^θ defined in (2.20) is well-defined, bounded, non-linear and continuously Fréchet differentiable on $X \times W$ for each temperature. □

Note that the spatial H^2-regularity of solutions to piezoelectric system are needed in time-domain as well as in frequency-domain formulations, since the observation operator contains a boundary integral of spatial derivatives of the solution the to piezoelectric system.

2.3. **The resulting inverse problem and adjoint system.** To state the inverse problem, which aims at reconstructing the unknown parameter from observed data, we introduce the adjoint system. Since observations are usually contaminated with noise up to a noise level δ, we have given the positive noisy data $\tilde{y}^\delta_\theta \in \mathbb{R}^{|\mathcal{W}|}$, which we transform component wise logarithmically,

$$y^\delta_\theta := \log\left(\tilde{y}^\delta_\theta\right).$$

For the forward operator for each fixed temperature $\theta \in \Theta$

$$F^\theta : X \to \mathbb{R}^{|\mathcal{W}|}, \;\; F^\theta(p) = C^\theta(p, S^\theta(p)),$$

we want to identify $p \in X$ such that

$$F^\theta(p) = y^\delta_\theta. \tag{2.21}$$

Hence, the reduced approach casts the problem into an operator equation in $\mathbb{R}^{|\mathcal{W}|}$ for the sought-after quantity p. This problem is ill-posed in the sense of Hadamard, see [25], meaning the solution may not be unique or may not depend continuously on the data. Small perturbations in the measurement data y^δ_θ can lead to large deviations in the reconstructed parameter function p. Regularization is therefore essential to stabilize the solution process. Consequently, we introduce a weakly lower semi-continuous regularizer $\mathcal{R}_\tau : X \to \mathbb{R}$ with a regularization parameter $\tau > 0$. Then, we model the inverse problem similarly to [25] as an optimization problem. Hence, we aim at finding a minimizer of the regularized target functional $\mathcal{J} : X \to \mathbb{R}$ for each fixed $\theta \in \Theta$, which we assume to exist, where

$$\mathcal{J}(p) := J_\theta(p) + \mathcal{R}(p), \tag{2.22}$$

and

$$J_\theta(p) := \frac{1}{2}\left\|F^\theta(p) - y_\theta^\delta\right\|^2_{\mathbb{R}^{|\mathcal{W}|}}. \tag{2.23}$$

Using derivative-based methods necessitates gradient computation, which is often done via adjoints. Hence, unique existence of the adjoint state is desirable, as it can be seen as revealing the influence of a cause on a target functional. To obtain the adjoint PDE system of the piezoelectric system (2.11) - (2.14), we have to differentiate the model operator, see Definition 2.7, with respect to the state in the direction (d, ψ)

$$\begin{aligned}
&\frac{\mathrm{d}B((\hat{u}, \hat{\phi}_0), (v, w))}{\mathrm{d}\left(\hat{u}, \hat{\phi}_0\right)}(d, \psi) = \frac{\partial B((\hat{u}, \hat{\phi}_0), (v, w))}{\partial \hat{u}} d + \frac{\partial B((\hat{u}, \hat{\phi}_0), (v, w))}{\partial \hat{\phi}_0} \psi \\
&= 2\pi \int_\Omega -s_1 \rho \omega^2 d^\mathrm{T} \overline{v} + \left(s_2 c^\mathrm{E}(\theta) \mathcal{B} d + e(\theta)^\mathrm{T} \nabla \psi\right)^\mathrm{T} \overline{\mathcal{B} v} + \left(e(\theta)\mathcal{B} d - \epsilon^\mathrm{S}(\theta) \nabla \psi\right)^\mathrm{T} \overline{\nabla w} \, \mathrm{d}\Omega \, .
\end{aligned}$$

Denoting the adjoint state as $(q_1, q_2) \in H^2_{\mathcal{B}}(\Omega, \mathbb{C}^2) \times H^2_{0,\Gamma}(\Omega, \mathbb{C})$ yields

$$\begin{aligned}
&\frac{\mathrm{d}B((\hat{u}, \hat{\phi}_0), (q_1, q_2))}{\mathrm{d}\left(\hat{u}, \hat{\phi}_0\right)}(d, \psi) \\
&= 2\pi \int_\Omega -s_1 \rho \omega^2 d^\mathrm{T} \overline{q_1} + \left(s_2 c^\mathrm{E}(\theta) \mathcal{B} d + e(\theta)^\mathrm{T} \nabla \psi\right)^\mathrm{T} \overline{\mathcal{B} q_1} + \left(e(\theta)\mathcal{B} d - \epsilon^\mathrm{S}(\theta) \nabla \psi\right)^\mathrm{T} \overline{\nabla q_2} \, \mathrm{d}\Omega \\
&= 2\pi \int_\Omega \left(-s_1 \rho \omega^2 \overline{q_1} - \mathcal{B}^\mathrm{T}\left(s_2 c^\mathrm{E}(\theta) \mathcal{B}\overline{q_1} + e(\theta)^\mathrm{T} \nabla \overline{q_2}\right)\right)^\mathrm{T} - \nabla \cdot \left(e(\theta)\mathcal{B}\overline{q_1} - \epsilon^\mathrm{S}(\theta)\nabla\overline{q_2}\right)^\mathrm{T} \psi \, \mathrm{d}\Omega \\
&\quad + \underbrace{2\pi \int_\Gamma \mathcal{N} \cdot \left(s_2 c^\mathrm{E}(\theta)\mathcal{B}\overline{q_1} + e(\theta)^\mathrm{T}\nabla\overline{q_2}\right)^\mathrm{T} d \, \mathrm{d}\Gamma}_{\overset{!}{=}0} + \underbrace{2\pi \int_\Gamma n \cdot \left(e(\theta)\mathcal{B}\overline{q_1} - \epsilon^\mathrm{S}(\theta)\nabla\overline{q_2}\right)^\mathrm{T} \psi \, \mathrm{d}\Gamma}_{\overset{!}{=}0} \, .
\end{aligned}$$

Consequently, the adjoint system for $(q_1, q_2) \in H^2_{\mathcal{B}}(\Omega, \mathbb{C}^2) \times H^2_{0,\Gamma}(\Omega, \mathbb{C})$ is given by

$$\forall \omega \in \mathcal{W}: \;\; -\rho\omega^2 s_1 \overline{q_1} - \mathcal{B}^\mathrm{T}\left(s_2 c^\mathrm{E}(\theta)\mathcal{B}\overline{q_1} + e(\theta)^\mathrm{T}\nabla\overline{q_2}\right) = \frac{\partial J_\theta}{\partial \hat{u}} \quad \text{in } \Omega \tag{2.24}$$

$$-\nabla \cdot \left(e(\theta)\mathcal{B}\overline{q_1} - \epsilon^\mathrm{S}(\theta)\nabla\overline{q_2}\right) = \frac{\partial J_\theta}{\partial \hat{\phi}_0} \quad \text{in } \Omega \tag{2.25}$$

$$n \cdot \left(e(\theta)\mathcal{B}\overline{q_1} - \epsilon^\mathrm{S}(\theta)\nabla\overline{q_2}\right) = 0 \quad \text{on } \Gamma_n \tag{2.26}$$

$$\mathcal{N}^\mathrm{T}\left(s_2 c^\mathrm{E}(\theta)\mathcal{B}\overline{q_1} + e(\theta)^\mathrm{T}\nabla\overline{q_2}\right) = 0 \quad \text{on } \partial\Omega, \tag{2.27}$$

which is uniquely solvable for every state $(\hat{u}, \hat{\phi}_0) \in W$ due to Theorem 2.6. Hence, we obtain a unique adjoint state for each PDE solution and not only the existence of a Lagrangian multiplier (i.e., adjoint state) associated to a minimizer. The right-hand side of the adjoint system is the Fréchet derivative of the objective functional J for a fixed temperature with respect to the state variables. This term acts as the source for the adjoint system, propagating information about the data mismatch backwards through the model. We want to employ the *discretize-then-optimize* (DO) strategy for the actual calculation of the adjoint and hence, the gradient. However, the analysis of the continuous problem (2.24) - (2.27) is an indispensable prerequisite for the DO approach. Consequently, the well-posedness of the continuous adjoint problem, including the existence and uniqueness of the adjoint state, serves as the essential mathematical foundation.

3. THE BCD RSE-QN APPROACH

In practical solution approaches to inverse problems in piezoelectricity, sensitivities of the forward operator with respect to different parameters vary considerably, see [19], which is not desirable for solving inverse problems. For a better handling of sensitivities we propose a *block coordinate descent* (BCD) method, that was successfully used by [18] in the context of parameter identification problems in piezoelectricity. The basic idea of BCD methods is to obtain the solution of an optimization problem by solving a sequence of "smaller" optimization problems. Specifically, these algorithms are usually iterative methods in which the minimization of the objective functional with respect to a previously selected block consisting of components of the optimization variables is achieved in each iteration step, while the remaining components of the optimization variables are fixed to their values of the current iteration, see [31]. This block is then updated and fixed for the next block. On the one hand, the advantage is that each of these sub-problems is lower-dimensional than the original minimization problem and, on the other hand, regarding second-order methods, the degrees of freedom in the corresponding Hessian operators (or approximations thereof) are reduced, see [31]. To illustrate the approach, assume that $X \subset \mathbb{R}^n$ and choose for the optimization problem

$$\min_{p \in X} \mathcal{J}(p) \tag{3.1}$$

a block B_i^k containing coordinates with indices $b_i^k \subseteq \{1, 2, \ldots, n\}$, where k refers to the k-th iteration step and i to the block number in the k-th iteration step. Then, we update the corresponding sub-vector $p^{b_i^k} \in \mathbb{R}^{|b_i^k|}$ of the optimization variables, i.e.,

$$p_{k+1}^{b_i^k} = p_k^{b_i^k} + s_k,$$

where $s_k \in \mathbb{R}^{|b_i^k|}$ is typically a descent direction of the lower dimensional sub-problem. With $I_{b_i^k}$ denoting the $|b_i^k| \times |b_i^k|$ dimensional identity matrix embedded in $\mathbb{R}^{n \times |b_i^k|}$, we can reformulate the BCD update as

$$p^{k+1} = p^k + I_{b_i^k} s_k,$$

see [28]. The next block B_{i+1}^k is chosen according to $b_{i+1}^k \subseteq \{1, 2, \ldots, n\} \setminus \cup_{l=1}^i b_l^k$. There are different ways to realize the BCD method, and therefore to define the block B_i^k as well as the direction s_k. Firstly, we need a strategy to select an appropriate b_i^k. Possibilities for this choice would be to fix certain disjoint partitions of $\{1, 2, \ldots, n\}$ with a prescribed cardinality a-priori. This means that we cycle through the same partitions every time, which is known as cyclic selection and refers to the Gauss-Seidel method for linear systems. Next, one could choose the block size and the coordinates therein in each iteration, which is called variable block selection. Therefore, blocks can be chosen from all possible subsets of $\{1, 2, \ldots, n\}$ randomly or with greedy approaches where an underlying optimization problem must be solved to obtain the optimal block. If the iteration costs are high, then greedy BCD versions are too costly. Furthermore, [28] suggests using fixed blocks over variable blocks, Newton-type methods for each block and larger and fewer blocks if the iteration cost does not increase heavily. Since, e.g., [18], also recommends to apply Newton-type methods in the context of parameter identification problems in piezoelectricity, we will use the RSE-PSB, see [23]. This can be seen as a "corrected" Levenberg-Marquardt method or a regularized structure-exploiting *Quasi-Newton* (QN) method especially designed for solving inverse problems, where second order derivative information is desirable because of non-linearity or cross-sensitivity information. By computing the Hessian of $\mathcal{J}$ defined in (2.22), i.e.,

$$H(p_k) := F'(p_k)^* F'(p_k) + F''(p_k)^* \left(F(p_k) - y^\delta \right) + \tau_k I,$$

one obtains the regularized Newton method,

$$H(p_k)(p_{k+1} - p_k) = F'(p_k)^* \left(y^\delta - F(p_k) \right),$$

where we omit the superscript corresponding to the temperature for the sake of readability. Computing H directly is numerically very costly. Hence, the idea is to use QN methods, but those methods often do not take the structure of $\mathcal{J}$ and H into account. Therefore, if we assume that F' is known or easily accessible, analogously to the Levenberg-Marquardt (LM) method, only

$$Z(p_k) := F''(p_k)^* \left(F(p_k) - y^\delta \right)$$

is difficult and expensive to compute. Consequently, the goal is to find A_k such that $A_k \approx Z(p_k)$. One possibility is to set $A_k = 0$ for all $k \in \mathbb{N}$, which corresponds to the LM method, but the approximation error is only small if F is linear or the residual is sufficiently small, i.e., we have a good approximation and an initial guess close to the optimum. In real-world applications obtaining such an initial guess can be very challenging. Therefore, the idea of the RSE-PSB method is to employ QN updates for A_k. Note that even the specific QN method has to be chosen carefully, as Z may not be positive definite, while still symmetric. Consequently, we focus on the PSB update and define the residual r_k and the step s_k as,

$$r_k := F(p_k) - y^\delta,\ s_k := p_{k+1} - p_k.$$

A Taylor approximation leads to the following modified secant condition,

$$(F''(p_k)^* r_k)s_k = (F'(p_{k+1}) - F'(p_k))^* r_{k+1},\ \text{ yielding }\ y_k := (F'(p_{k+1}) - F'(p_k))^* r_{k+1}.$$

Then, we obtain the PSB update to approximate $F''(p_k)^* r_k$ via

$$A_{k+1} = A_k + \frac{(y_k - A_k s_k) \otimes s_k + s_k \otimes (y_k - A_k s_k)}{\langle s_k, s_k \rangle} - \frac{\langle y_k - A_k s_k, s_k \rangle s_k \otimes s_k}{\langle s_k, s_k \rangle^2},$$

where $\otimes$ denotes the outer product. Hence, using the PSB update for computing A_k and

$$\mathcal{B}_k := F'(p_k)^* F'(p_k) + A_k + \tau_k I$$

as approximation operator to $H(p_k)$ yields the RSE-PSB method

$$\mathcal{B}_k(p_{k+1} - p_k) = F'(p_k)^* \left(y^\delta - F(p_k)\right).$$

Thus, the RSE-PSB method leverages the problem structure not only by decomposing in data discrepancy and regularization terms but also by exploiting the structure of the analytical second Fréchet derivative of the respective regularized target functional. To ensure the regularization property as well as robustness in practical applications, particularly when the initial guess significantly deviates from the true solution, and to have a concrete choice of the regularization parameter, [23] adapted an approach from [20]. The latter approach controls the regularization parameter such that it leads to globalization in a finite dimensional setting. Therefore, the control approach also serves as an a-priori rule to choose the regularization parameter. This strategy yields a globalization technique, ensuring convergence towards a local minimizer even when the initial guess p_0 is far from the true solution. We combine this QN approach with a cyclic BCD

Algorithm 1 BCD-GRSE algorithm

```
Require: $k = 0; c, a, \mu \in (0,1); \sigma > 1; p_0 \in \mathbb{R}^n; y^\delta \in \mathbb{R}^{|\mathcal{W}|}; b_i \subseteq \{1, 2, \dots, n\} \setminus \cup_{l=1}^{i-1} b_l;$
         $A_0^i \in \mathbb{R}^{|b_i| \times |b_i|}; \tau_0^i > 0; g_0^i > \eta^i, i = 1, \cdots, m.$
  while $g_k^i > \eta^i$ for all $i = 1, \cdots, m$ do
      for $i = 1, \cdots, m$ do
          Evaluate $F(p_k)$, compute $F'_{b_i}(p_k)$, $r_k = F(p_k) - y^\delta$, $J'_{b_i}(p_k) = F'_{b_i}(p_k)^* r_k$.
          if $k > 0$: then
              Set $\check{p}_k \leftarrow (p_k^1, \cdots, p_k^{i-1}, p_{k-1}^i, p_k^{i+1}, \cdots p_k^m)$, compute $F'_{b_i}(\check{p}_k)$ and $A_k^i$ with RSE-PSB.
          end if
          If eq. (3.2) is solvable: Compute $s_k$ as solution of
(3.2)             $\left(F'_{b_i}(p_k)^* F'_{b_i}(p_k) + A_k^i + \tau_k^i I\right) s_k = -J'_{b_i}(p_k).$
          Compute $\text{pred}_k = \frac{\tau_k^i}{2} \|s_k\|^2 - \frac{1}{2} J'_{b_i}(p_k)^T s_k,\ \text{ared}_k = J_{b_i}(p_k) - J_{b_i}(p_k + s_k),\ \rho_k = \frac{\text{ared}_k}{\text{pred}_k}$.
          while $\rho_k \leq c$ or $\text{pred}_k \leq a g_k \|s_k\|$ : do
              if eq. (3.2) is not solvable then
                  Set $\tau_k^i \leftarrow \sigma \tau_k^i$
              else
                  Solve eq. (3.2) for $s_k$ and compute $\text{pred}_k = \frac{\tau_k^i}{2} \|s_k\|^2 - \frac{1}{2} J'_{b_i}(p_k)^T s_k$,
                  $\text{ared}_k = J_{b_i}(p_k) - J_{b_i}(p_k + s_k),\ \rho_k = \frac{\text{ared}_k}{\text{pred}_k}$.
              end if
          end while
          Update $\hat{p}_k^i \leftarrow p_k^i + s_k$ and $p_k \leftarrow (\hat{p}_k^1, \cdots, \hat{p}_k^{i-1}, \hat{p}_k^i, p_k^{i+1}, \cdots p_k^m)$
          Set $\tau_{k+1}^i \leftarrow \mu \tau_k^i$ and compute $g_{k+1}^i = \left\| J'_{b_i}(p_k) \right\|$
      end for
      Update $p_{k+1} \leftarrow (\hat{p}_k^1, \cdots, \hat{p}_k^m)$ and $k = k + 1$
  end while
```

method. Therefore, the blocks do not change during the optimization process, i.e., $b_k^i = b^i$. We denote $m < n$ as the number of blocks and $\dot{\bigcup}_{i=1}^m b_i = \{1, 2, \dots, n\}$. The resulting BCD-GRSE algorithm that employs the dynamic control of the regularization parameter as presented in [23] is shown in Algorithm 1. For this purpose, we denote $p_k := (p_k^1, \cdots, p_k^m)$ corresponding to the blocks $b_1, \cdots, b_m$. Conditioning the decrease of the regularization parameters on the first occurrence of convergence in the preceding blocks can enhance stability in practical applications. An open question is which parameters should be grouped together in one block. Thus, we want to tackle the problem of coordinate choice and having different sensitivity values by a sensitivity driven partitioning approach. For this purpose, we analyze the sensitivities and cross-sensitivities. The sensitivity of a quantity can be understood as a measure of the change in this quantity when certain influences change. The cross-sensitivity measures the potential for mutual influence between two specific parameters in relation to changes in a specific quantity. Hence, sensitivities of an operator are understood as derivatives. We define normalized parameters

$$x_i := \frac{p_i}{\|p_i\|} \quad \Rightarrow \quad p_i = x_i \|p_i\|$$

and reformulate the function $F(p)$ to

$$F(p) = F(x_1\|p_1\|, \dots, x_{10}\|p_{10}\|) = \tilde{F}(x).$$

The partial derivative of $\tilde{F}$ with respect to x_i is obtained using the chain rule

$$\frac{\partial \tilde{F}}{\partial x_i} = \frac{\partial F}{\partial p_i} \cdot \frac{\partial p_i}{\partial x_i} = \|p_i\| \frac{\partial F}{\partial p_i},$$

which measures the sensitivity relative to the respective scale. This approach corresponds to the logarithmic differential and thus to the sensitivity in terms of elasticity theory, i.e., the percentage change in F for a percentage change in p_i. The normalization is crucial because parameters may have different physical units and magnitudes. Without normalization, a direct comparison of their derivatives would be less reasonable.

Definition 3.1. We define the partial sensitivity of the forward operator with respect to a certain parameter $x_j,\ j \in \{1, \dots, n\}$, as

$$\left\{ \frac{\partial \tilde{F}_\omega(x)}{\partial x_j} \right\}_{\omega \in \mathcal{W}} = \left\{ C'_{\omega_x}(x, S(x)) S'(x) \right\}_{\omega \in \mathcal{W}}, \tag{3.3}$$

the sensitivity κ_j of the forward operator with respect to a certain parameter $x_j,\ j \in \{1, \dots, n\}$, as

$$\{\kappa_{j,\omega}(x)\}_{\omega \in \mathcal{W}} := \left\{ \left| \frac{\partial \tilde{F}_\omega(x)}{\partial x_j} \right| \right\}_{\omega \in \mathcal{W}} \tag{3.4}$$

with

$$\kappa := \begin{pmatrix} \kappa_{1,1} & \cdots & \kappa_{1,\omega_{|\mathcal{W}|}} \\ \vdots & \ddots & \vdots \\ \kappa_{n,1} & \cdots & \kappa_{n,\omega_{|\mathcal{W}|}} \end{pmatrix} \in \mathbb{R}^{n \times |\mathcal{W}|} \tag{3.5}$$

the sensitivity matrix, and the total sensitivity V_j of the forward operator with respect to a certain parameter $x_j,\ j \in \{1, \dots, n\}$, as

$$V_j(x) := \sum_{\omega \in \mathcal{W}} \kappa_{j,\omega}(x). \tag{3.6}$$

Furthermore, we define the cross-sensitivity $\xi^{j,l}$ of the forward operator with respect to the parameter x_j and $x_l,\ j, l \in \{1, \dots, n\},\ j \neq l$, as

$$\xi^{j,l}(x) := \sum_{\omega \in \mathcal{W}} \left| \frac{\partial}{\partial x_l} \left(\frac{\partial \tilde{F}_\omega(x)}{\partial x_j} \right) \right|. \tag{3.7}$$

A high value of the cross-sensitivity $\xi^{j,l}$ indicates that a change in parameter x_l significantly alters the sensitivity of the model to parameter x_j. In the context of optimization, this means that the gradient with respect to x_j is highly dependent on the value of x_l. Sensitivities may also be defined differently, for instance via second-order difference quotients or statistically through conditional expectations and variances, see [26]. The pairwise parameter coupling via cross-sensitivities is encoded in the strictly upper triangular matrix

$$\xi(x) = \begin{pmatrix} 0 & \xi^{1,2} & \xi^{1,3} & \cdots & \xi^{1,n} \\ 0 & 0 & \xi^{2,3} & \cdots & \xi^{2,n} \\ \vdots & \vdots & \ddots & \ddots & \vdots \\ 0 & 0 & \cdots & 0 & \xi^{n-1,n} \\ 0 & 0 & \cdots & 0 & 0 \end{pmatrix}, \tag{3.8}$$

where each entry $\xi^{j,l},\ j < l$, quantifies the cross-sensitivity between parameters x_j and x_l. It can be understood as a structural measure of pairwise interactions between model parameters. Specifically, off-diagonal entries $\xi^{j,l},\ j < l$, quantify the cross-sensitivity between parameters x_j and x_l and hence the parameter coupling and interaction. Due to the assumed smoothness, $\xi(x)$ could also be chosen as symmetric matrix. However, the strictly upper triangular representation of $\xi(x)$ is motivated to avoid redundancy in encoding pairwise parameter interactions. Hence, we avoid to duplicate information that could lead to double counting in subsequent aggregation steps. To capture directional sensitivity interactions that go beyond pairwise effects, we introduce a scalar, curvature-based measure derived from second-order derivatives of the objective function. For each block b_k, we define the intra-block roughness measure of the gradient as

$$\hat{\xi}_{b_k}(x) := \frac{1}{V_{b_k}(x)} \sum_{i,j \in b_k} \xi^{i,j} \quad \text{for } k \in \{1, \cdots, m\}, \tag{3.9}$$

where

$$V_{b_k}(x) := \sum_{i \in b_k} V_i(x) \quad \text{for } k \in \{1, \cdots, m\} \tag{3.10}$$

denotes the total first-order sensitivity of block b_k. We reasonably assume that this first-order block sensitivity is strictly positive, otherwise the parameters in the corresponding block would have no influence on the forward operator at all. Therefore, $\hat{\xi}_{b_k}$ measures the rate at which the gradient of the objective function changes along the directions in b_k, normalized by first-order sensitivity in that direction, which specifies the inter-block roughness of the gradient. High values of $\hat{\xi}_{b_k}(x)$ identify directions exhibiting strong non-linearity or potential numerical instability. Consequently, one may see this quantity as local condition number. The intra-block roughness measure $\hat{\xi}_{b_k}(x)$ can be intuitively understood as an average non-linearity measure of the problem within the parameter subspace defined by block b_k. A block with low roughness is desirable because the optimization sub-problem associated with it will be better conditioned. Additionally, each quantity $\hat{\xi}_{b_k}(x)$ can be identified as sensitivity of the gradient to small perturbations in parameters of block b_k, which can be seen as the normalized cross-sensitivity. In the context of BCD, we aim to form parameter groupings that have a stable gradient in terms of roughness and are externally as decoupled as possible, where the latter is certainly more important. We consider a partition into non-trivial, disjoint blocks. Let the set of all admissible m-partitions be defined as

$$\mathcal{P}_m := \left\{ P \subset \mathcal{P}(\{1, \ldots, n\}) : \dot{\cup}_{i=1}^{m} b_{\iota_i} = \{1, \ldots, n\} \right\}, \tag{3.11}$$

where $\mathcal{P}$ denotes the power set. To guarantee external decoupling, we define the inter-block coupling as the total cross-sensitivity across two blocks in a specific $P \in \mathcal{P}_m$ as

$$\xi_{b_k,b_l}(x) := \sum_{i \in b_k} \sum_{j \in b_l} \xi^{i,j}(x). \tag{3.12}$$

To determine optimal parameter blocks, we minimize a composite objective function that combines inter-block cross-sensitivity with the intra-block roughness measure,

$$\min_{P \in \mathcal{P}_m} w_1 \sum_{b_k \in P} \hat{\xi}_{b_k}(x) + w_2 \sum_{b_k \in P} \sum_{b_l \in P} \xi_{b_k,b_l}(x), \tag{3.13}$$

where $w_1, w_2 \in \mathbb{R}_{\geq 0}$ are pre-defined weights representing the trade-off between interaction across the blocks and the roughness within each block. The choice of weights w_1 and w_2 governs the nature of the partitioning. It is reasonable to emphasize the inter cross-sensitivity between blocks, i.e., we choose weights $w_1, w_2 \in [0, 1]$ with $w_1 \ll w_2$ and $w_1 = 1 - w_2$. This framework supports the identification of parameter blocks with low internal curvature variability and minimal coupling across the blocks. Minimizing the first term ensures that blocks are composed of parameters with small roughness in the gradient, i.e., with approximately linear or mildly non-linear sensitivity structures. The second term penalizes the interaction across the blocks. Once blocks are formed, the total first-order sensitivity of the blocks may guide the prioritization of block updates during the BCD update, for instance by selecting the block with highest total first-order sensitivity first. Since $|\mathcal{P}_m|$ denotes the number of ways to partition n parameters into m blocks, it grows rapidly with n and m. It is related to the Stirling numbers of the second kind as it can be seen as general graph partitioning problem of a complete weighted graph. Hence, it is useful to deal with small dimensions, where exhaustive enumeration can be used. Then, the proposed curvature-based framework provides an approach to structural decomposition of parameter spaces and offers a refined view of coupling, non-linearity, and stability. For larger dimensions greedy heuristics, spectral methods or relaxation approaches would be necessary.

4. SOLUTION OF THE INVERSE PROBLEM WITH SYNTHETIC DATA AND CONSTANT TEMPERATURE

4.1. **General numerical setting.** To perform a valuable analysis of the sensitivities and to solve the inverse problem, it is necessary to implement a suitable numerical model. For this purpose, we use the DO approach, where the problem setting is discretized first. Then, the analysis of the sensitivities and the optimization are performed within this finite-dimensional setting. Specifically, the spatial discretization is realized using a classical *finite element method* (FEM) implemented in the FEM tool FEniCS [1] (dolfin version 2019.2.0.dev0). The gradient-based optimization methods including the sensitivity computations described in the previous sections require easy access to first order Fréchet derivatives as accurate and consistent as possible in a computationally measurable sense. To obtain these accurate derivatives efficiently, we employ *algorithmic differentiation* (AD) [16] via the dolfin-adjoint [27] library (version 2019.1.0), which integrates seamlessly with FEniCS. The central concept is that the computation of a discretized operator can be decomposed into a finite sequence of elementary operations such as addition, multiplication and elementary function calls. By calculating the derivatives with respect to the arguments of these operations, one has the necessary tool to systematically apply the chain rule to arrive at the derivatives of the entire sequence of operations with respect to the input variables. Hence, we obtain consistent first-order derivatives of high precision [15]. AD operates in two primary modes, namely the forward mode, which propagates derivatives forward together with the function evaluation and the reverse mode, which propagates derivatives backward. The reverse mode of AD is related to solving the discrete adjoint of the discretized forward problem, see e.g., [3], where AD automatically generates and solves the discrete adjoint problem, providing accurate gradients required for the optimization algorithms. As domain Ω we consider a rectangle with vertices $(2.6, 0)$, $(6.35, 0)$, $(6.35, 1)$, and $(2.6, 1)$, where coordinates are given in mm, which corresponds to a ring-shaped geometry, see Figure 1, with outer radius of $6.35\,\mathrm{mm}$, inner radius of $2.6\,\mathrm{mm}$ and thickness of $1\,\mathrm{mm}$. Furthermore, we use $\hat{\phi}^{\mathrm{e}} = 0.03\,\mathrm{V}$ as excitation and perform any numerical realization in kHz. This has the advantage of a better condition of the PDE system, as the elastic stiffness parameter is down-scaled with 10^{-6}, the piezoelectric coupling parameter is up-scaled with 10^{3} and the permittivity parameter is up-scaled with 10^{12}, yielding that the magnitudes of the material parameters differ significantly less. The material parameters and damping parameters selected for the FEM simulations are presented in Table 1. The damping parameters α and β as given in Table 1 are used throughout the remainder of this paper. The element size h and the polynomial order g are the key factors in determining the frequency at which this configuration is suitable, and the numerical deviations that are to be expected above that frequency. According to [17], it is possible to specify a frequency

$$f < \left(g + \frac{1}{2}\right) \frac{1}{\pi h} \sqrt{\frac{c^{\mathrm{D}}}{\rho}} \tag{4.1}$$

for which the model delivers satisfactory results. A comparison of the numerical deviation of the results and the computational time indicates that an element size of $h = 150\,\mathrm{\mu m}$ and a polynomial order of

TABLE 1. Material parameters from [10] used for numerical computation.

Parameter	Value	Parameter	Value
c_{11}	$151.4\,\mathrm{GPa}$	ϵ_{33}	$5.5\,\mathrm{nF\,m^{-1}}$
c_{12}	$132.7\,\mathrm{GPa}$	e_{15}	$9.4\,\mathrm{C\,m^{-1}}$
c_{13}	$83.6\,\mathrm{GPa}$	e_{31}	$-5.2\,\mathrm{C\,m^{-1}}$
c_{33}	$128.8\,\mathrm{GPa}$	e_{33}	$13.9\,\mathrm{C\,m^{-1}}$
c_{44}	$25.9\,\mathrm{GPa}$	α	$37.8\,\mathrm{ms^{-1}}$
ϵ_{11}	$2.7\,\mathrm{nF\,m^{-1}}$	β	$42\,\mathrm{fs}$

$g = 3$ yield sufficiently reasonable simulation outcomes. Using inequality (4.1), $c^{\mathrm{D}} = 170\,\mathrm{GPa}$ and $\rho = 7850\,\mathrm{kg\,m^{-3}}$ for a PIC181 piezoceramic [29], this results in a frequency of $f < 34.56\,\mathrm{MHz}$, which suits the assumed frequency range. Consequently, this configuration is employed for the subsequent computations. Furthermore, specifying the Dirichlet lift function $\hat{\chi}$ in the system (2.11) - (2.14) is not necessary and can be avoided in practice, as it is possible to directly implement mixed Dirichlet conditions in FEniCS.

4.2. **Sensitivity analysis.** This section details the sensitivity analysis performed to understand how the forward model's output is influenced by variations in each material parameter. The results of this analysis directly motivate the sensitivity-driven block partitioning strategy for the BCD algorithm that follows. From [10] conclusions can be drawn about the reasonable frequency domains for the inverse problem. Therein it is emphasized that the range between the first radial resonance and the capacitive range between the first and second thickness resonance is particularly suitable for parameter identification. Hence, we will use the range from $1\,\mathrm{kHz}$ to $6000\,\mathrm{kHz}$ with step-size of $10\,\mathrm{kHz}$, i.e.,

$$\mathcal{F}_{\mathrm{g}} := \{f \in \mathbb{N} : \ f \equiv 0 \bmod 5,\ f \leq 6000\}, \quad \mathcal{W}_{\mathrm{g}} := \{\omega = 2\pi f \in \mathbb{R}^+ : f \in \mathcal{F}_g\}. \tag{4.2}$$

To effectively visualize and compare the sensitivities, we introduce two normalization schemes that scale the sensitivity matrix. We will scale the partial sensitivities on the one hand, with normalization of one sensitivity for all angular frequency points after the respective (row-wise) maximum and, on the other hand, of all sensitivities for one angular frequency point after the respective (column-wise) maximum. Then, we obtain the matrices

$$\kappa^{\mathrm{rm}} := \begin{pmatrix} \frac{\kappa_{1,1}}{\max_{\omega\in\mathcal{W}_{\mathrm{g}}} \kappa_{1,\omega}} & \cdots & \frac{\kappa_{1,\omega_{|\mathcal{W}|}}}{\max_{\omega\in\mathcal{W}_{\mathrm{g}}} \kappa_{1,\omega}} \\ \vdots & \ddots & \vdots \\ \frac{\kappa_{10,1}}{\max_{\omega\in\mathcal{W}_{\mathrm{g}}} \kappa_{10,\omega}} & \cdots & \frac{\kappa_{10,\omega_{|\mathcal{W}|}}}{\max_{\omega\in\mathcal{W}_{\mathrm{g}}} \kappa_{10,\omega}} \end{pmatrix}, \qquad \kappa^{\mathrm{cm}} := \begin{pmatrix} \frac{\kappa_{1,1}}{\max_j \kappa_{j,1}} & \cdots & \frac{\kappa_{1,\omega_{|\mathcal{W}|}}}{\max_j \kappa_{j,\omega_{|\mathcal{W}|}}} \\ \vdots & \ddots & \vdots \\ \frac{\kappa_{10,1}}{\max_j \kappa_{j,1}} & \cdots & \frac{\kappa_{10,\omega_{|\mathcal{W}|}}}{\max_j \kappa_{j,\omega_{|\mathcal{W}|}}} \end{pmatrix}. \tag{4.3}$$

Ideally, all partial sensitivities would be similar and close to one, but this is by no means realistic in practical applications, as the sensitivities depend, among other things, on the overall geometry of the ceramic itself, which will not be changed. One can try to increase sensitivities either via a sensitivity optimization or via optimal experiment design of electrode configurations, see [19]. The BCD approach is an alternative that does not change, but provides better handling of sensitivities. For the subsequent sensitivity results, we used the parameters in Table 1, chose the angular frequency grid $\mathcal{W}_{\mathrm{g}}$ defined in (4.2) and used AD for first- and second-order sensitivity computations. In Figure 2 we see the illustration of the matrices in (4.3), where the black points indicate those sensitivities $\kappa_{j,\omega}$ over $\mathcal{W}_{\mathrm{g}}$ which are higher than 90 % of $\max_{\omega\in\mathcal{W}_{\mathrm{g}}} \kappa_{j,\omega}$ for each $j \in \{1, \dots, 10\}$. The row-wise normalization (κ^{rm}, left in Figure 2) highlights the frequency-dependent profile of each parameter's sensitivity relative to its own maximum. For example, c_{11} and c_{33} exhibit sharp peaks near the material's resonance frequencies. Conversely, the column-wise normalization (κ^{cm}, right in Figure 2) illustrates which parameter dominates at a specific frequency. The existing approaches to group parameters enforce to categorize them in similar frequency domain regions. This means that parameters are grouped together, which have high sensitivity at a specific frequency range and optimize them on that range, while keeping them fixed at other ranges, see [6]. Nevertheless, the interaction between those parameters in a specific range can be high. We do not follow that approach of domain splitting, as we emphasize reducing the inter cross-sensitivities and use a BCD approach instead of a pure coordinate descent approach as in [10]. As mentioned before, the sensitivities of the forward operator in piezoelectric inverse parameter identification problems can vary strongly, which is illustrated also in Figure 3. Since the cross-sensitivity analysis is especially useful for the block choice in the subsequent inverse problem, we

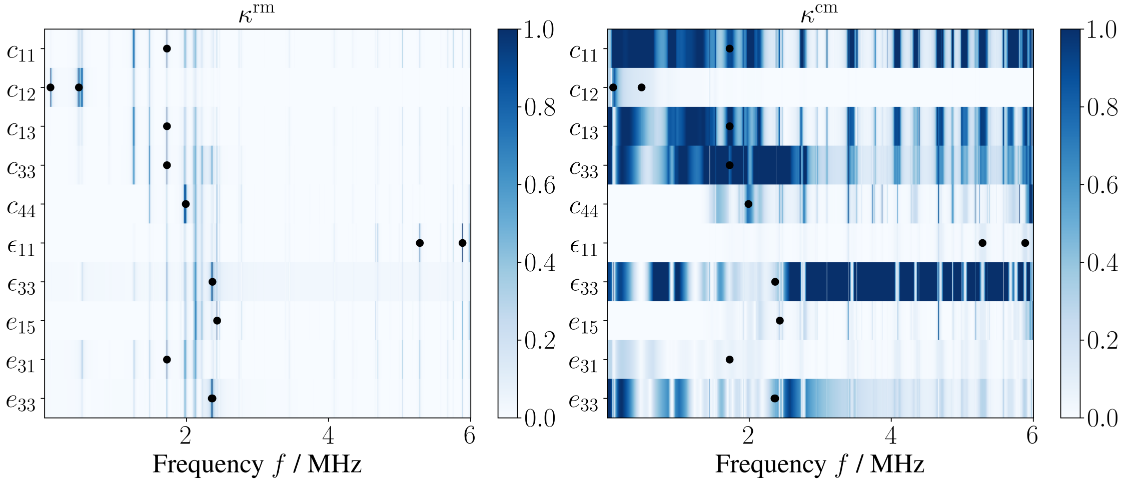

FIGURE 2. Row-wise and column-wise normalized sensitivities κ^{rm} and κ^{cm} with respect to the parameters in Table 1 on $\mathcal{W}_{\mathrm{g}}$.

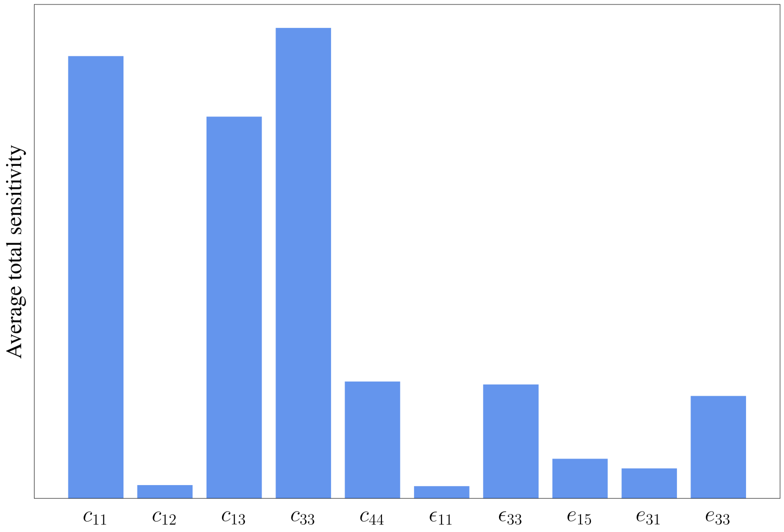

FIGURE 3. Total average sensitivities of the forward operator with respect to the parameters in Table 1 on $\mathcal{W}_{\mathrm{g}}$.

assume the same numerical configurations. Specifically, we use the same spatial mesh, initial parameters and angular frequency domain grid for the solution to the inverse problem (2.23) and for the solution to the combinatorial block choice problem (3.12). We specify as initial guess p_0 the parameters in Table 1 with 5% overestimation. To dampen any amplification of the discrepancy in sensitivities by the forward operator we select a suitable angular frequency range, see [24]. From Figure 2, conclusions can be drawn about reasonable frequency domains for the inverse problem. Due to the small sensitivities of the forward operator with respect to c_{12} and ϵ_{11}, we use a fine angular frequency grid in areas where the forward operator is more sensitive to those parameters and in resonance areas. In the other parts of the angular frequency domain we use a coarse grid. Hence, with the frequency domains

$$\mathcal{F}_1 := \{f \in \mathbb{N} : \ f \equiv 0 \bmod 3, \ 38 \leq f < 2600\}, \quad \mathcal{F}_2 := \{f \in \mathbb{N} : \ f \equiv 0 \bmod 20, \ 2600 \leq f < 4500\},$$
$$\mathcal{F}_3 := \{f \in \mathbb{N} : \ f \equiv 0 \bmod 3, \ 4500 \leq f \leq 6000\},$$

we consider

$$\mathcal{W}_{\mathrm{a}} := \{\omega = 2\pi f \in \mathbb{R}^+ : \ f \in \mathcal{F}_1 \cup \mathcal{F}_2 \cup \mathcal{F}_3\} \tag{4.4}$$

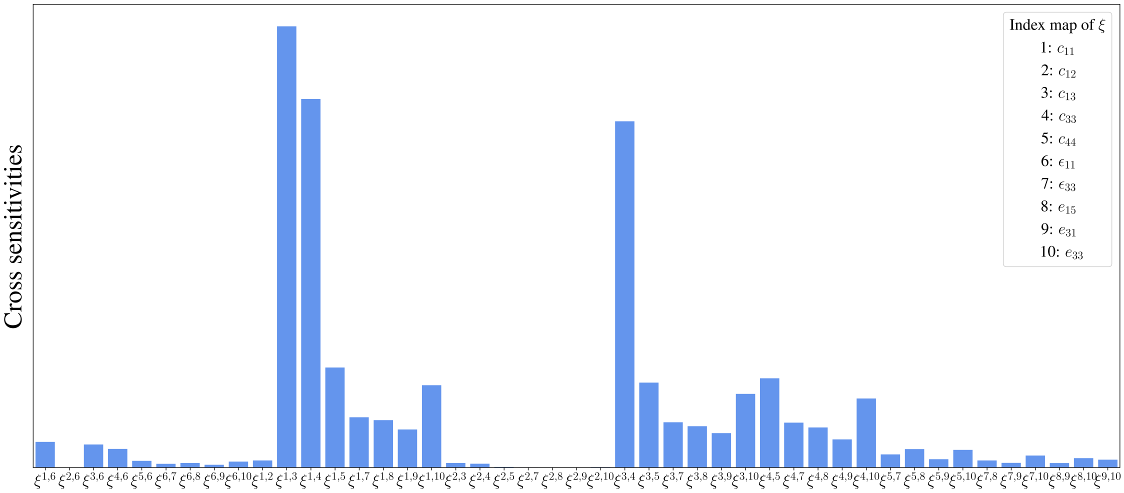

FIGURE 4. Total cross-sensitivities of the forward operator with parameters in Table 1 and 5% overestimation on $\mathcal{W}_{\mathrm{a}}$.

as angular frequency domain. This adaptive selection concentrates computational effort in angular frequency regions rich with information, while sparsely sampling regions where the model is less sensitive. This can be viewed as a form of a-posteriori experimental design, optimizing the data used for the inversion rather than the physical experiment itself. Furthermore, this results in the advantage of less computations in the sensitivity analysis as the cardinality of the angular frequency domain became smaller. With this approach we obtain the cross-sensitivities, c.f. identity (3.8), for all parameters as shown in Figure 4, illustrating clearly the disparity in cross-sensitivities. The bars corresponding to pairs like (c_{11}, c_{13}) and (c_{11}, c_{33}) represent strong interactions where a change in one parameter drastically alters the gradient with respect to the other. Unadapted optimization algorithms could struggle with such a landscape, as the search direction would be compromised by these conflicting influences.

Since we want to reconstruct $n = 10$ material parameters, we have $\mathcal{I} = \{1, 2, \dots, 10\}$ as the index set of parameters for a fixed $\theta \in \Theta$ in our concrete application. As detailed above, we will use a cyclic BCD-GRSE method and consider a bipartition, i.e., $m = 2$, into two non-trivial, mutually disjoint blocks,

$$b_1 \subset \mathcal{I}, \quad b_2 = \mathcal{I} \setminus b_1, \quad \text{with} \quad 2 \leq |b_1|, |b_2| \leq 8. \tag{4.5}$$

Consequently, the problem of determining optimal parameter blocks can be simplified to

$$\min_{\substack{b_1 \subset \mathcal{I} \\ 2 \leq |b_1| \leq 8}} w_1 \left(\hat{\xi}_{b_1}(x) + \hat{\xi}_{b_2}(x) \right) + w_2 \cdot \xi_{b_1, b_2}(x). \tag{4.6}$$

Since $n = 10$ and $m = 2$, we use exhaustive enumeration to solve problem (4.6), where we chose $w_1 = 0.1$ and $w_2 = 0.9$, resulting in the partition $b_1 = \{c_{11},\ c_{13},\ c_{33},\ c_{44},\ \epsilon_{33},\ e_{15},\ e_{31},\ e_{33}\}$, $b_2 = \{c_{12},\ \epsilon_{11}\}$. Computing the total first-order sensitivity of each block suggests that we prioritize b_1. This partitioning is also supported by the intuitive approach of combining the two parameters with the lowest overall sensitivity (c_{12} and ϵ_{11}) into a separate block. However, this intuitive strategy would not necessarily be effective, as inter-block correlations may still be high. The advantage of our approach is that we are able to reasonably conclude that the parameter blocks exhibit small interaction and the dominant parameters are isolated.

4.3. **Solution to the simulation-based inverse problem.** To validate the performance of the proposed BCD-GRSE algorithm and the effectiveness of the sensitivity-based block partitioning strategy, we first conduct a numerical experiment using synthetic data. To generate the noisy data y^δ we contaminate the exact simulated data y, generated according to the parameters in Table 1, additively with uniformly distributed random noise with a noise level of 2%. As initial guess p_0 we used the parameters in Table 1 with 5% overestimation. Additionally, we performed numerical tests using a 5% underestimated initial guess, which yielded similar convergence results.

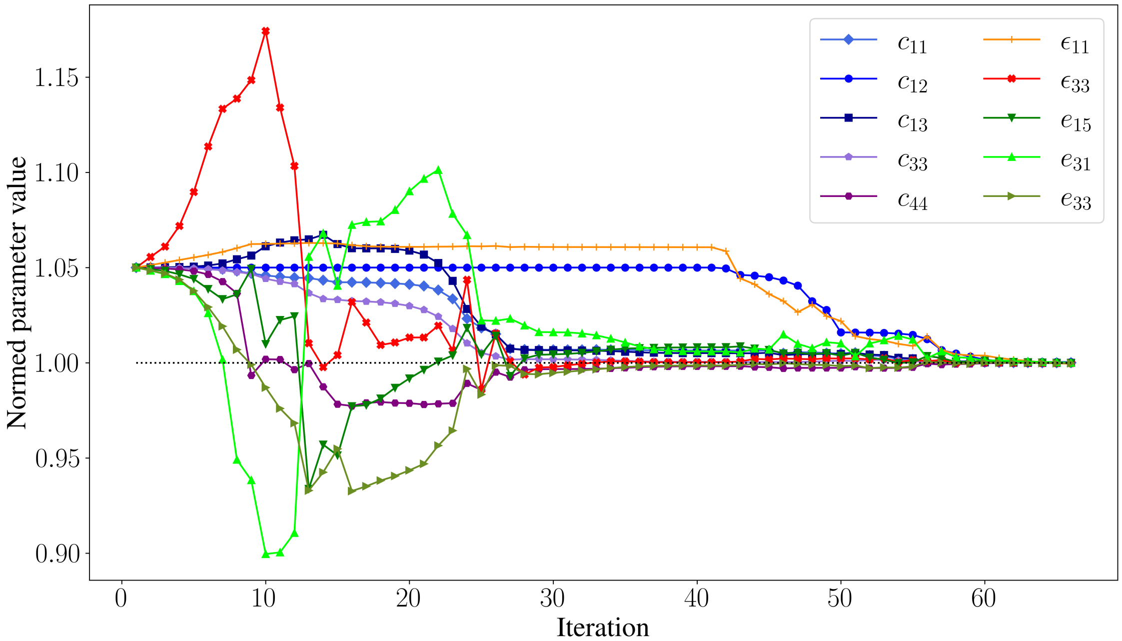

FIGURE 5. BCD-GRSE parameter identification from simulated noisy data.

We employ the hyperparameters $\mu = 0.5$, $\tau_0^1 = \tau_0^2 = 10^{-3}$, $\sigma = 4$, $c = a = 10^{-2}$ and $\eta^1 = 5\eta^2$, $\eta^2 = 1.45 \cdot 10^{-5}$. For improved stability, the regularization parameter of the second block was reduced when the norm of the first-block update dropped below 1 for the first time. Here, μ is the decay factor and σ is the growth factor of the regularization parameters for each block, see [23], and $c,\ a$ refer to $c,\ p$ in [23]. As initial Quasi-Newton matrices for each block we use $F''(p_0)^* \left(F(p_0) - y^\delta\right)$, where $F''(p_0)$ is computed via AD. Figure 5 shows the parameter identification performance of the BCD-GRSE method. For the sake of better visualization, the reconstructed parameter values have been normalized with the respective true parameter, so that convergence to the value 1 is desired. The reconstruction results in Figure 5 show successful convergence to the true parameters in Table 1, even for the least sensitive parameters c_{12} and ϵ_{11}. The successful reconstruction from noisy synthetic data provides numerical evidence for the proposed method and validates the sensitivity-driven block decomposition strategy. Note that throughout the iterative optimization process, every iteration step remained in the feasible set.

5. APPLICATION TO EXPERIMENTAL MEASUREMENT DATA

5.1. **Experimental Setup.** After the validation of the proposed method using synthetic data, the subsequent step is its application to real measurement data. The behaviour of a piezoceramic sample under varying temperature conditions is investigated through the measurement of its electrical impedance at these conditions. The experimental configuration is fundamentally reliant upon a temperature-controlled chamber, in which the sample under test is securely positioned. This chamber is designed to ensure a constant thermal environment for the samples during the impedance measurement. Temperature regulation is achieved via a precise thermostat system (*Magio MS-310F, Julabo, Germany*). At each temperature point within a specified range of 25 °C to 85 °C in increments of 5 °C, electrical impedance measurements are conducted using an impedance analyser (*E4990A, Keysight Technologies, USA*). Ventilation is implemented to ensure uniform temperature distribution within the chamber, thereby minimising temperature gradients across the sample. Both the thermostat and the impedance analyser are computer-controlled, enabling automated measurements to be conducted across the entire temperature range. A sufficient time period of half an hour is implemented to allow the sample to reach thermal equilibrium with the chamber. The examined specimen is a PIC181 (*PI Ceramic, Germany*) annular piezoelectric ceramic with dimensions that correspond to those previously described in Section 4 and shown in Figure 1. For the identification of the temperature-dependent material parameters based on the measurements, we assume an equidistant discretization of Θ with $5\,^\circ\mathrm{C}$ - step-size between $25\,^\circ\mathrm{C}$ and $85\,^\circ\mathrm{C}$, analogous to the measurements, yielding $\Theta := \{25, 30, 35, 40, 45, 50, 55, 60, 65, 70, 75, 80, 85\}$. As the data measured at each temperature is a vector consisting of absolute values of the impedance, i.e.,

$$|Z_\omega(p,z)| := \left| \frac{-\hat{\phi}^{\mathrm{e}} Q^i_\omega(p,z)}{\omega |Q_\omega(p,z)|^2} + i \frac{-\hat{\phi}^{\mathrm{e}} Q^r_\omega(p,z)}{\omega |Q_\omega(p,z)|^2} \right| = \frac{\hat{\phi}^{\mathrm{e}}}{\omega |Q_\omega(p,z)|^2} \left| Q^i_\omega(p,z) + Q^r_\omega(p,z) \right| = \frac{\hat{\phi}^{\mathrm{e}}}{\omega |Q_\omega(p,z)|}$$

we equivalently convert it according to the forward operator via

$$|Q_\omega(p,z)| = \frac{\hat{\phi}^{\mathrm{e}}}{\omega |Z_\omega|(p,z)}$$

resulting in

$$y^\delta_\omega := \log\left(\frac{\hat{\phi}^{\mathrm{e}}}{\omega |Z_\omega|_{\mathrm{meas}}} \right).$$

The angular frequency grid for the reconstruction is chosen as in Section 4. Then, for each fixed temperature we have to reconstruct a different set of material parameters. We start by reconstructing the material parameters at $25\,^\circ\mathrm{C}$, where we use the parameters given in Table 1 as initial parameters. Since the material properties at a given temperature are assumed to be independent of the properties at other temperatures, the inverse problem can be solved independently for all remaining temperatures. This allows the application of a trivial parallelization of the characterization process. Consequently, after obtaining the results for $25\,^\circ\mathrm{C}$, given in the first column of Table 2, we use those parameters as initial parameters for all remaining $\theta \in \Theta$. We expect on the one hand that this approach yields a better initial guess and on the other hand significantly faster convergence. Furthermore, we employed the same hyperparameters as in subsection 4.3 and used $F''(p_0)^* \left(F(p_0) - y^\delta\right)$, where $F''(p_0)$ is computed via AD, as initial Quasi-Newton matrices.

5.2. **Results based on measurement data.** Applying the BCD-GRSE algorithm to the experimental data for each temperature $\theta \in \Theta$ yields the values of the parameters as depicted in Table 2, with elasticity parameter components in GPa, piezoelectric coupling parameter components in $\mathrm{C\,m^{-1}}$ and permittivity parameter components in $\mathrm{nF\,m^{-1}}$, rounded to three decimal places. Comparing the data misfit for each temperature achieved by the BCD-GRSE algorithm to the results presented in [12] confirms that our method consistently achieves less than half of the data misfit values of [12], which can be seen in Table 3. A visual comparison of the measured data, the data generated with the reconstructed parameters using the BCD-GRSE algorithm and the data from [12] showed almost indistinguishable results across the temperature domain. Therefore, we chose results for the representative temperature of $50\,^\circ\mathrm{C}$, illustrated in Figure 6. For better visualization, the first row shows zoomed-in versions of the grey-marked characteristic regions

TABLE 2. Results of the parameter identification for each $\theta \in \Theta$ based on real measurement data applying the BCD-GRSE algorithm.

θ \ p_j	c_{11}	c_{12}	c_{13}	c_{33}	c_{44}	ϵ_{11}	ϵ_{33}	e_{15}	e_{31}	e_{33}
25	140.866	72.667	78.466	129.929	28.213	8.595	5.580	11.673	-5.468	14.102
30	140.997	73.131	78.539	130.023	28.252	8.912	5.651	11.825	-5.473	14.238
35	141.197	73.451	78.668	130.034	28.227	8.741	5.723	11.788	-5.473	14.356
40	141.456	73.958	78.816	130.027	28.203	8.582	5.811	11.761	-5.495	14.467
45	141.579	74.177	78.883	130.044	28.207	8.543	5.890	11.789	-5.519	14.548
50	141.527	74.104	78.865	130.142	28.206	8.557	5.990	11.811	-5.576	14.625
55	141.244	73.550	78.688	130.193	28.233	8.585	6.087	11.819	-5.626	14.729
60	141.076	73.294	78.556	130.234	28.319	8.923	6.184	11.971	-5.656	14.871
65	141.252	73.786	78.530	130.232	28.642	10.502	6.293	12.711	-5.581	15.097
70	141.513	74.344	78.582	130.179	28.608	10.246	6.376	12.598	-5.567	15.213
75	141.761	74.853	78.680	130.128	28.498	9.575	6.480	12.334	-5.622	15.305
80	141.260	73.665	78.430	130.300	28.608	10.033	6.578	12.503	-5.680	15.402
85	141.269	73.872	78.384	130.432	28.728	10.649	6.698	12.762	-5.711	15.554

TABLE 3. Data misfit values using reconstructed mat. parameters in Table 2 compared to data misfit values using mat. parameters of [12] and the relative improvement to [12].

Temperature θ / °C	J_θ using material parameter in [12]	J_θ using material parameter in Table 2	Relative improvement to [12] in %
25	19.976	8.203	58.94%
30	19.463	7.877	59.53%
35	18.770	7.379	60.69%
40	17.904	6.812	61.95%
45	17.035	6.373	62.59%
50	16.821	6.379	62.08%
55	17.122	6.614	61.37%
60	16.863	6.459	61.70%
65	16.299	5.845	64.14%
70	15.900	5.435	65.82%
75	16.130	5.895	63.45%
80	15.653	5.872	62.49%
85	15.771	5.737	63.62%

in Figure 6. The reconstructed data corresponding to row 6 in Table 2 align closely with the measurements, validating the accuracy of the identified parameter set presented in Table 2. Notably, the regions containing the most information, i.e., the resonance and anti-resonance areas, show strong a agreement between the BCD-GRSE reconstructed data and the measurements. Furthermore, the BCD-GRSE reconstruction provides a substantially better fit to the measurements than the results from [12], as indicated by Table 3, which is particularly visible in these regions. The slight mismatch in the peak amplitudes may be attributed to the Rayleigh damping model, which does not fully capture all material loss mechanisms, suggesting the need for further model refinement.

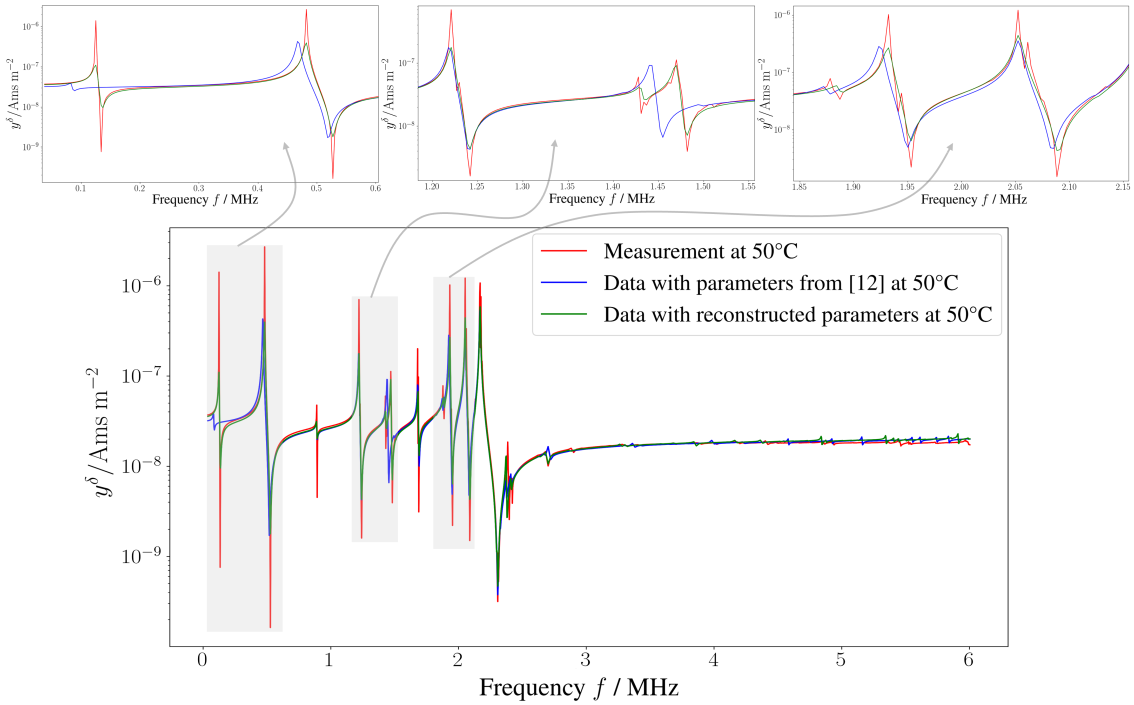

FIGURE 6. Simulation using reconstructed material parameters compared to simulation using data in [12] and measured data at 50 °C, zooming in on the characteristic resonance and anti-resonance regions.

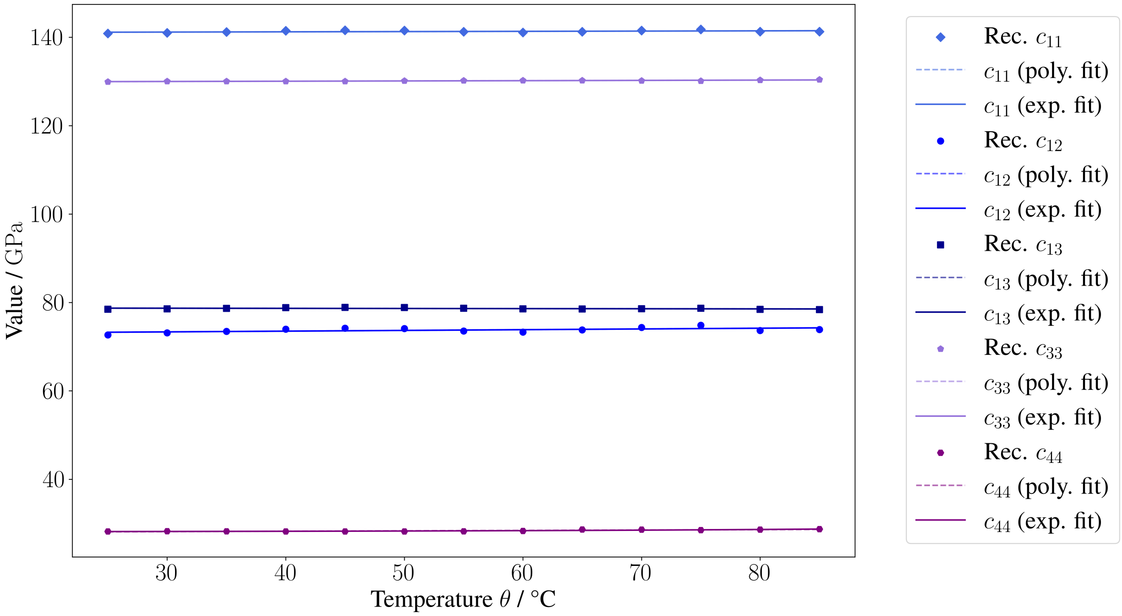

FIGURE 7. Reconstructed temperature-dependent material behavior of c^{E} with first order polynomial fit (dashed lines) and exponential fit (solid lines).

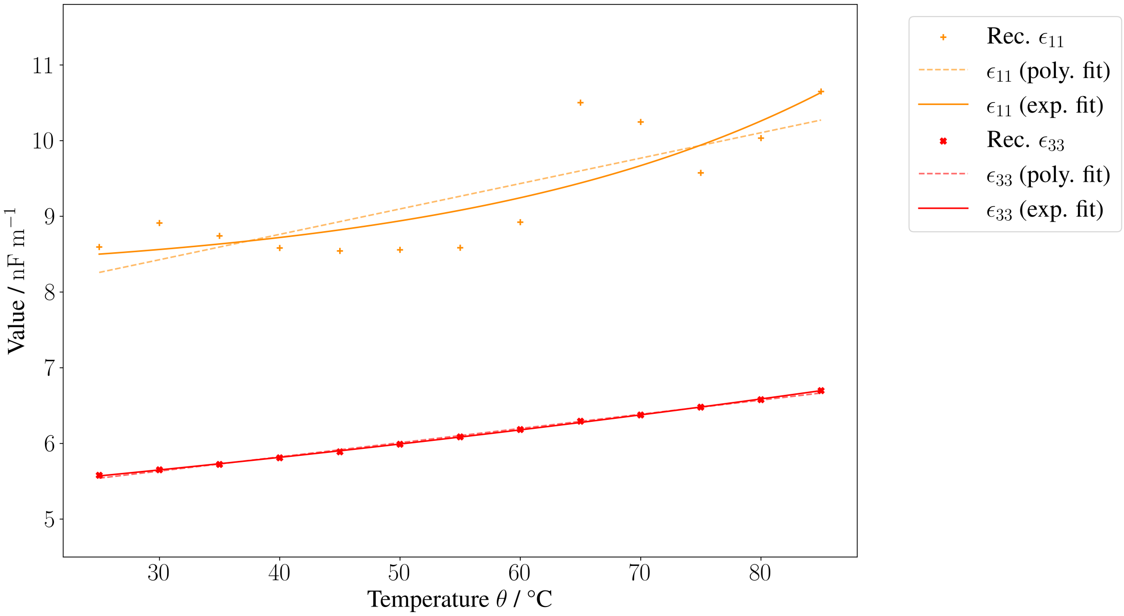

FIGURE 8. Reconstructed temperature-dependent material behavior of ϵ^{S} with first order polynomial fit (dashed lines) and exponential fit (solid lines).

To obtain continuous functions representing the temperature dependency of each parameter, we perform an exponential curve approximation on the values in Table 2 and additionally fit a first order polynomial regression model to these values. The advantage of an exponential fit is that we obtain a monotone function, which is a reasonable behavior, while still giving opportunities for possible nonlinearities. Figures 7, 8 and 9 show the identified temperature dependency of the elastic, piezoelectric, and dielectric parameters, respectively. The points represent the discrete values from Table 2, the solid lines represent the exponential

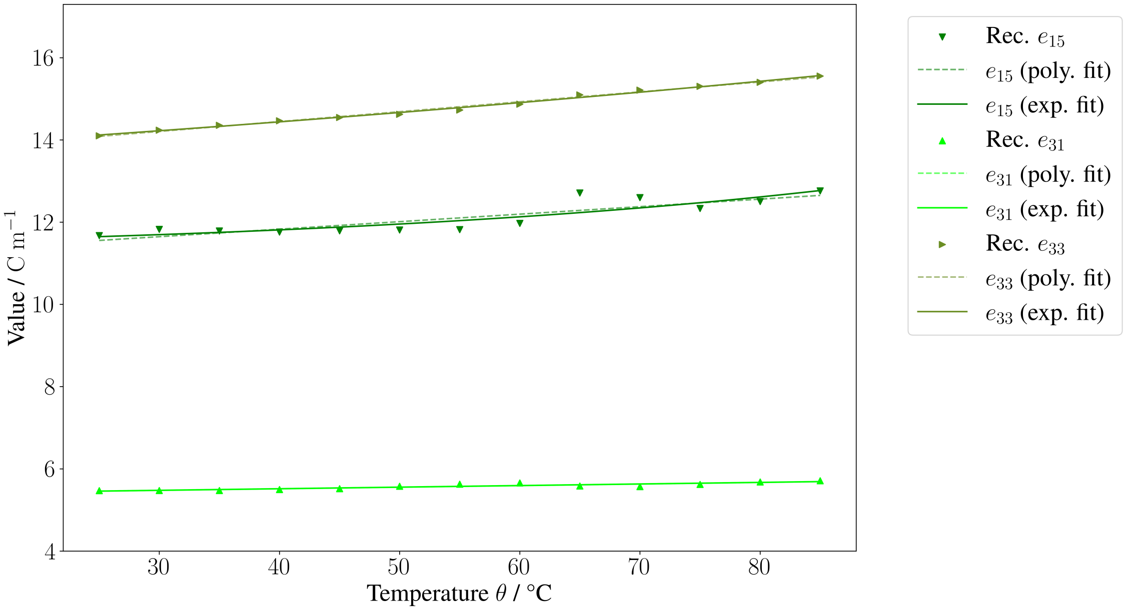

FIGURE 9. Reconstructed temperature-dependent material behavior of e with first order polynomial fit (dashed lines) and exponential fit (solid lines).

curve fit and the dashed lines the fitted polynomial functions of first order. The identified parameters in Figures 7, 8 and 9 show clear trends with increasing temperature. The elastic stiffness parameters (Figure 7) exhibit a nearly constant behavior with a negligible slope as temperature rises. Conversely, the permittivity and piezoelectric coupling components demonstrate significant temperature dependence. In Figure 8, a pronounced linear increase is observed for the permittivity parameter $\epsilon_{33}(\theta)$. Similarly, as shown in Figure 9, the piezoelectric coupling parameter functions $e_{15}(\theta)$, $e_{31}(\theta)$ and $e_{33}(\theta)$ follow a linear trend. However, $\epsilon_{11}(\theta)$ exhibits a slight non-linear behavior. One factor that could contribute to the non-linearity observed in $\epsilon_{11}(\theta)$ is that the forward operator is least sensitive to this specific parameter. This observation has been made also in previous contributions [10], and consequently, it appears to be more challenging to identify the parameter function $\epsilon_{11}(\theta)$. To quantify the sensitivity of each parameter function to temperature changes and the non-linearity with respect to temperature, the C-norm (maximum absolute value) of

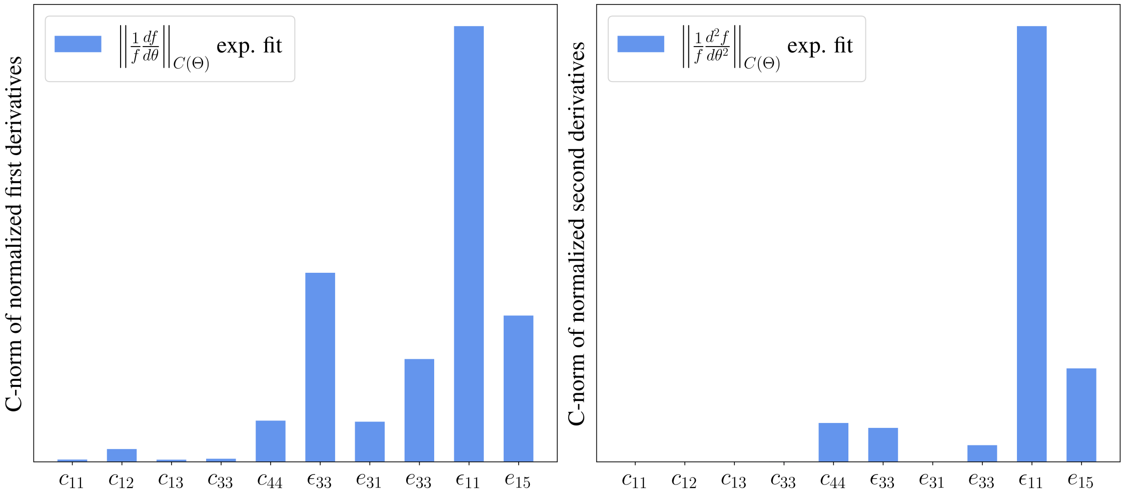

FIGURE 10. C-norm of normalized first and second derivatives of the exponential parameter functions.

the normalized first and second derivatives of the exponential curves to each parameter function are illustrated in Figure 10. The C-norm of the normalized first derivatives (left in Figure 10) essentially serves as a thermal sensitivity measure, quantifying the rate of change for each material property. It confirms that especially the permittivity and the piezoelectric coupling parameters are sensitive to temperature changes, while the elasticity parameter remains more stable. However, $c_{44}(\theta)$ seems to be the most temperature dependent elasticity parameter. The right plot in Figure 10 encourages the distinction between seemingly linear and non-linear parameter functions. The seemingly non-linear function $\epsilon_{11}(\theta)$ exhibits high C-norm sensitivity and curvature values, which supports the hypothesis that the observed non-linearity arises from a combination of the low sensitivity of the identification process for these parameters and potential physical effects. In contrast, the seemingly linear parameters possess low C-norm curvature values relative to $\epsilon_{11}(\theta)$. Finally, the identified parameter sets for all temperatures satisfy the thermodynamic stability conditions outlined in Definition 2.3, additionally ensuring physically plausibility.

6. CONCLUSION AND OUTLOOK

In this paper, we presented a framework for identifying temperature-dependent piezoelectric material parameters from charge measurements in the frequency domain. We formulated the forward problem in an axisymmetric environment and analyzed the corresponding inverse problem. To address the strong parameter coupling and sensitivities across very different orders of magnitude, we introduced a sensitivity-informed block construction strategy within a block coordinate descent algorithm. The block structure was derived from first- and second-order sensitivity measures, including total sensitivities, cross-sensitivities, and a curvature-based roughness indicator. This systematic analysis allowed us to algorithmically partition the parameter space into two blocks that reduce the coupling between parameters while maintaining numerical stability. To address the ill-posedness we used the GRSE method to update each block. Numerical experiments with noisy synthetic data have shown that all ten piezoelectric material parameters can be reliably reconstructed, including those with very low sensitivity. Finally, we applied the sensitivity-informed BCD-GRSE framework to real charge measurements of a single ring-shaped PIC181 sample over a temperature range of $25\,^{\circ}\mathrm{C}$ to $85\,^{\circ}\mathrm{C}$. The match between the simulation with the reconstructed material parameters and the measurement data has been improved and is satisfactorily accurate. In addition, the reconstructed material parameters exhibit physically plausible temperature dependencies and remained feasible. In summary, the determined material parameters represent plausible solutions to the inverse problem and can thus be considered representative of the real ceramic in the sense of the applied FEM model. As a result, the proposed approach provides a robust and theoretically sound method for determining piezoelectric parameters under realistic measurement conditions. Future work will focus on the investigation of piezoelectric systems under electrical load and mechanical stress as external influences besides temperature. Our approach can be applied in this setting, as the method is independent of temperature. This can lead to the identification of the relevant correlations, thus facilitating a more in-depth understanding and modeling of the non-linear behavior that occurs during the operation of piezoelectric components.

ACKNOWLEDGMENTS

The authors would like to thank the German Research Foundation (DFG) for financial support within the research group 5208 NEPTUN (444955436). The work on this paper was partly funded by the Deutsche Forschungsgemeinschaft (DFG, German Research Foundation) under Germany´s Excellence Strategy – The Berlin Mathematics Research Center MATH+ (EXC-2046/1, EXC-2046/2, project ID: 390685689).

REFERENCES

[1] M. Alnæs et al. “The FEniCS project version 1.5”. In: *Archive of Numerical Software* 3 (2015).
[2] F. Anderl and M. Mayle. “Sensitivity analysis of piezoelectric material parameters using Sobol indices”. In: *tm - Technisches Messen* 92.6 (Apr. 2025), pp. 234–242. ISSN: 2196-7113.
[3] O. Burghardt et al. “Coupled discrete adjoints for multiphysics in SU2”. In: *AIAA 2020-3139* (2020).
[4] J. Cerdà. *Linear functional analysis*. Vol. 116. American Mathematical Soc., 2010.
[5] L. Claes et al. “Machine learning-supported inverse measurement procedure for broadband, temperature dependent piezoelectric material parameters”. In: *Acta Acustica* 9.65 (Oct. 2025).

[6] N. Feldmann. “Ein modellbasiertes Messverfahren zur Charakterisierung von Piezokeramiken unter Verwendung eines einzelnen scheibenförmigen Probekörpers”. diss. Paderborn University, 2021.

[7] N. Feldmann et al. “An inverse approach to the characterisation of material parameters of piezoelectric discs with triple-ring-electrodes”. In: *tm - Technisches Messen* 86.2 (2019), pp. 59–65.

[8] N. Feldmann et al. “Inverse piezoelectric material parameter characterization using a single disc-shaped specimen”. In: *tm - Technisches Messen* 87.s1 (2020), s50–s55.

[9] N. Feldmann et al. “Modelling damping in piezoceramics: A comparative study”. In: *tm - Technisches Messen* 88.5 (2021), pp. 294–302.

[10] O. Friesen et al. “Estimation of piezoelectric material parameters of ring-shaped specimens”. In: *tm - Technisches Messen* (2024).

[11] O. Friesen et al. “Estimation of piezoelectric material parameters under varying electric field conditions”. In: *DAS / DAGA 2025 - 51st Annual Meeting on Acoustics*. 2025, pp. 994–997.

[12] O. Friesen et al. “Estimation of temperature-dependent piezoelectric material parameters using ring-shaped specimens”. In: *Journal of Physics: Conference Series* 2822.1 (2024), p. 012125.

[13] O. Friesen et al. “Sensitivity analysis and material parameter estimation of a pre-stressed Langevin transducer”. In: *2025 ICU, Paderborn, Germany*. AMA Service GmbH, 2025, pp. 138–141.

[14] O. Friesen et al. “Untersuchung piezoelektrischer Materialeigenschaften unter hydrostatischer Last”. In: *Fortschritte der Akustik - DAGA 2024*. 2024, pp. 1117–1120.

[15] R. Griesse and A. Walther. “Evaluating gradients in optimal control: continuous adjoints versus automatic differentiation”. In: *J. Optim. Theory Appl.* 122 (2004), pp. 63–86.

[16] A. Griewank and A. Walther. *Evaluating derivatives*. Second edition. SIAM, 2008.

[17] A. Hauck. “Higher order finite elements for coupled and anisotropic field problems”. diss. Erlangen, Friedrich-Alexander-Universität Erlangen-Nürnberg, 2016.

[18] B. Jurgelucks. “Increased sensitivity in parameter identification problems for piezoelectrics”. diss. Paderborn University, 2019.

[19] B. Jurgelucks et al. “Optimization of triple-ring electrodes on piezoceramic transducers using algorithmic differentiation”. In: *Optimization Methods and Software* 33.4-6 (2018), pp. 868–888.

[20] C. Kanzow and D. Steck. “Regularization of limited memory quasi-Newton methods for large-scale nonconvex minimization”. In: *Mathematical Programming Computation* 15.3 (2023), pp. 417–444.

[21] V. Karunakaran and V. Baby Thilaga. “Plancherel Theorem for vector valued functions and boehmians”. In: *The Rocky Mountain Journal of Mathematics* 28.4 (1998), pp. 1321–1342.

[22] R. Kuess, D. Walter, and A. Walther. *Modelling and analysis of an inverse parameter identification problem in piezoelectricity*. Technical Report. arXiv, 2026. URL: `https://optimization-online.org/?p=%20TEST`.

[23] R. Kuess and A. Walther. *On regularized structure exploiting Quasi-Newton methods for inverse problems*. Technical Report. Optimization Online, 2025. URL: `https://optimization-online.org/?p=29842`.

[24] R. Kuess et al. “Identification of temperature-dependent material parameter functions in piezoelectricity”. In: *2025 ICU, Paderborn, Germany*. AMA Service GmbH, 2025, pp. 134–137.

[25] T. Lahmer. “Forward and inverse problems in piezoelectricity”. diss. Friedrich-Alexander-Universität Erlangen-Nürnberg (FAU), 2008.

[26] T. Lahmer, J. Ilg, and R. Lerch. “Variance-based sensitivity analyses of piezoelectric models”. In: *Computer Modeling in Engineering & Sciences* 106.2 (2015), pp. 105–126.

[27] S. Mitusch, S. Funke, and J. Dokken. “dolfin-adjoint 2018.1: automated adjoints for FEniCS and Firedrake”. In: *Journal of Open Source Software* 4.38 (2019), p. 1292.

[28] J. Nutini, I. Laradji, and M. Schmidt. “Let’s make block coordinate descent converge faster: faster greedy rules, message-passing, active-set complexity, and superlinear convergence”. In: *J. Mach. Learn. Res.* 23.1 (2022).

[29] PI Ceramic GmbH. *Material data: Specific parameters of standard materials*. Aug. 2025.

[30] C. Scheidemann et al. *Influence of temperature and pre-Stress on the piezoelectric material behavior of ring-shaped ceramics*. International Conference on Functional Materials & Devices 2023 and 7th International Conference on Advanced Electromaterials. 2023.

[31] S.J. Wright. “Coordinate descent algorithms”. In: *Math. Programming* 151.1 (2015), pp. 3–34.